iScience

CellPress
OPEN ACCESS

Article

Human Dopaminergic Neurons Lacking PINK1 Exhibit Disrupted Dopamine Metabolism Related to Vitamin B6 Co-Factors

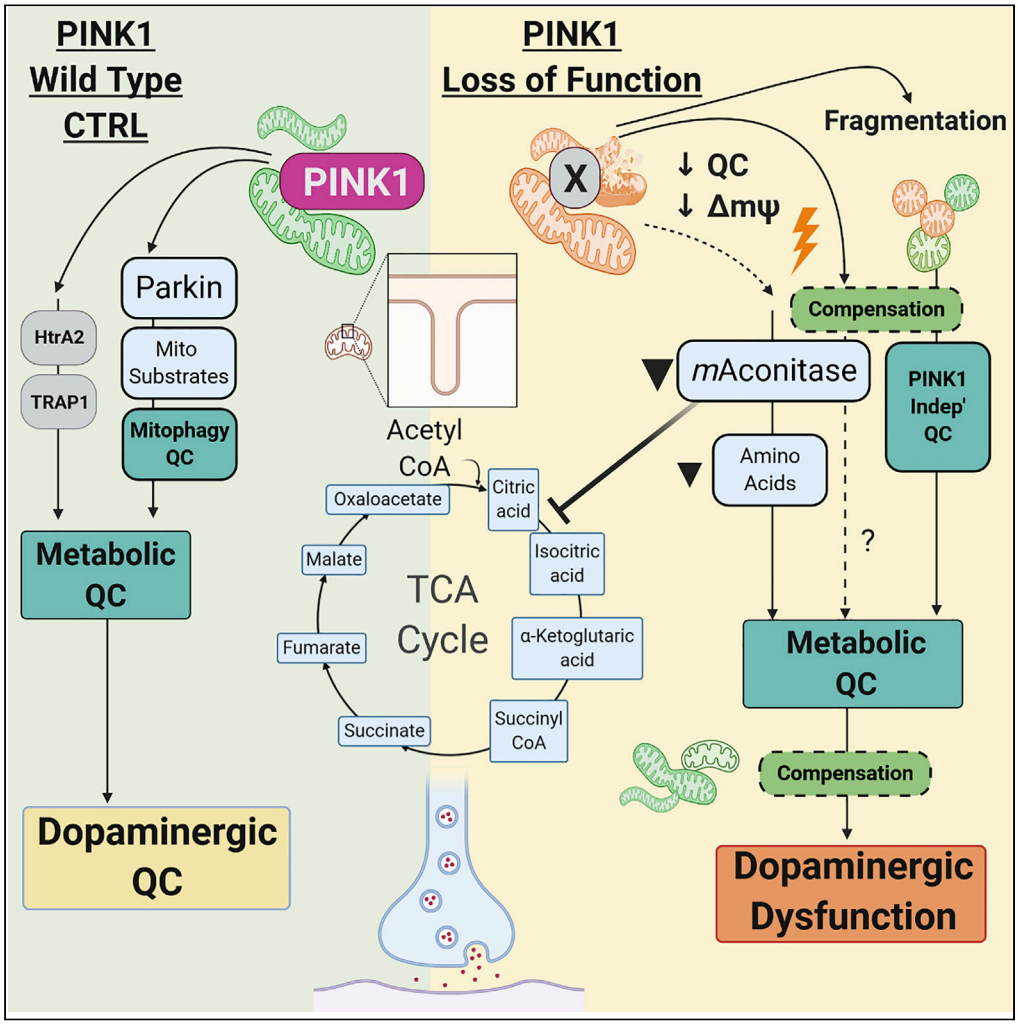

Christine Bus, Laimdota Zizmare, Marita Feldkaemper, ..., Christoph Trautwein, Christian J. Gloeckner, Julia C. Fitzgerald

julia.fitzgerald@uni-tuebingen.de

HIGHLIGHTS

PINK1 KO hDANs do not undergo ionophore-induced mitophagy yet CI remains active

PINK1 KO impacts the TCA cycle via *m*Aconitase leading to depletion of key amino acids

PINK1 KO silences *PNPO*, which provides essential biological co-factors

Dopamine pools and neurotransmitter uptake are reduced by PINK1 loss of function

Bus et al., iScience *23*, 101797
December 18, 2020 © 2020 The Authors.
https://doi.org/10.1016/j.isci.2020.101797

iScience

CellPress
OPEN ACCESS

Article

Human Dopaminergic Neurons Lacking PINK1 Exhibit Disrupted Dopamine Metabolism Related to Vitamin B6 Co-Factors

Christine Bus,[1,2,14] Laimdota Zizmare,[3,14] Marita Feldkaemper,[4] Sven Geisler,[1] Maria Zarani,[1] Anna Schaedler,[1,5] Franziska Klose,[6] Jakob Admard,[7] Craig J. Mageean,[2,6] Giuseppe Arena,[8] Petra Fallier-Becker,[9] Aslihan Ugun-Klusek,[10] Klaudia K. Maruszczak,[11] Konstantina Kapolou,[1,5] Benjamin Schmid,[1] Doron Rapaport,[11] Marius Ueffing,[4,6] Nicolas Casadei,[7] Rejko Krüger,[8,12] Thomas Gasser,[1,2] Daniela M. Vogt Weisenhorn,[13] Philipp J. Kahle,[1,2] Christoph Trautwein,[3] Christian J. Gloeckner,[2,6] and Julia C. Fitzgerald[1,15,*]

SUMMARY

PINK1 loss-of-function mutations cause early onset Parkinson disease. PINK1-Parkin mediated mitophagy has been well studied, but the relevance of the endogenous process in the brain is debated.

Here, the absence of PINK1 in human dopaminergic neurons inhibits ionophore-induced mitophagy and reduces mitochondrial membrane potential. Compensatory, mitochondrial renewal maintains mitochondrial morphology and protects the respiratory chain. This is paralleled by metabolic changes, including inhibition of the TCA cycle enzyme *m*Aconitase, accumulation of NAD$^+$, and metabolite depletion. Loss of PINK1 disrupts dopamine metabolism by critically affecting its synthesis and uptake. The mechanism involves steering of key amino acids toward energy production rather than neurotransmitter metabolism and involves cofactors related to the vitamin B6 salvage pathway identified using unbiased multi-omics approaches.

We propose that reduction of mitochondrial membrane potential that cannot be controlled by PINK1 signaling initiates metabolic compensation that has neurometabolic consequences relevant to Parkinson disease.

INTRODUCTION

PINK1 mutations are the second most frequent cause of early onset Parkinson disease (PD), and *PINK1* variants have been found in sporadic PD (Gandhi and Plun-Favreau, 2017; Klein et al., 2006). PINK1 PD has an early occurrence of L-DOPA-associated dyskinesia, slow disease progression, and absence of cognitive impairment (Schiesling et al., 2008; Valente et al., 2004). Affective and psychotic symptoms are also frequently a part of the clinical presentation (Steinlechner et al., 2007).

Homozygous *Pink1* knockout (KO) mice, *drosophila*, zebrafish, and PINK1 KO human cancer cells indicate that loss of PINK1 causes mitochondrial dysfunction, altered mitochondrial morphology, disturbed mitochondrial quality control, as well as iron and calcium toxicity (Esposito et al., 2013; Gautier et al., 2008; Gispert et al., 2009; Heeman et al., 2011; Julienne et al., 2017; Moisoi et al., 2014; Parganlija et al., 2014; Requejo-Aguilar et al., 2014; Villa et al., 2017; Vives-Bauza et al., 2010). PINK1 *in vivo* models are phenotypically mild, with neurodegeneration only observed in PINK1 KO zebrafish (Anichtchik et al., 2008; Soman et al., 2017). Dopamine release and synaptic plasticity alterations have been reported in *PINK1* KO mouse striatum (Kitada et al., 2007).

PINK1 is a serine/threonine kinase targeted to mitochondria acting in a pathway together with another PD gene product, the E3-ubiquitin ligase Parkin (Clark et al., 2006; Park et al., 2006), to regulate mitophagy (Geisler et al., 2010; Narendra et al., 2008, 2010a). Upon loss of mitochondrial membrane potential or accumulation of misfolded proteins, PINK1 stabilizes on the outer mitochondrial membrane (Jin et al., 2010; Jin and Youle, 2013; Narendra et al., 2010a). PINK1 then phosphorylates ubiquitin at Ser65 to activate Parkin (Kane et al., 2014; Kazlauskaite et al., 2014; Koyano et al., 2014). Parkin ubiquitinylates mitochondrial outer

[1]Department of Neurodegenerative Diseases, Centre of Neurology and Hertie Institute for Clinical Brain Research, University of Tübingen, Otfried Müller Strasse 27, 72076, Tübingen, Germany

[2]DZNE – German Center for Neurodegenerative Diseases, Tübingen, Germany

[3]Werner Siemens Imaging Center, Department of Preclinical Imaging and Radiopharmacy, University of Tübingen, Tübingen, Germany

[4]Institute for Ophthalmic Research, Centre for Ophthalmology, University of Tübingen, Tübingen, Germany

[5]Graduate School of Cellular and Molecular Neuroscience, University of Tübingen, Tübingen, Germany

[6]Core Facility for Medical Bioanalytics, University of Tübingen, Center for Ophthalmology, Institute for Ophthalmic Research, Tübingen, Germany

[7]NGS Competence Center Tübingen, Institute of Medical Genetics and Applied Genomics, University of Tübingen, Germany

[8]Translational Neuroscience, Luxembourg Centre for Systems Biomedicine (LCSB), University of Luxembourg, Luxembourg

[9]Institute of Pathology and Neuropathology, University of Tübingen, Tübingen, Germany

[10]School of Science and Technology, Nottingham

Continued

membrane proteins such as Mitofusins (Gegg et al., 2010) and Miro (Birsa et al., 2014). Miro1 is also suggested to be phosphorylated by PINK1 and is important for mitochondrial movement and arrest (Wang et al., 2011b). The buildup of ubiquitin chains on the outer mitochondrial membrane acts as a signal for the recruitment of autophagy receptors (Geisler et al., 2010; Lazarou et al., 2015; Wong and Holzbaur, 2014) important for mitochondrial clustering (Narendra et al., 2010b; Okatsu et al., 2010). Some *in vivo* studies have shown that PINK1 is not required for basal mitophagy in neurons (McWilliams et al., 2018; Lee et al., 2018) or in human platelets (Walsh et al., 2018) but the topic is controversial (for an extensive review see Chu, 2019; Cummins and Gotz, 2018).

The pathogenic action of PINK1 mutations could be cell-type specific. PINK1 is highly expressed in the brain but it is also expressed throughout the rest of the body and has been associated with disease mechanisms in several tissues (Wang et al., 2018; Guo et al., 2019) including the progression of some cancers (Berthier et al., 2011; Villa et al., 2017). PINK1 is expressed predominantly in neurons (Blackinton et al., 2007) and myelinating oligodendrocytes (Zhang et al., 2014b). First studies in PINK1 PD patient stem-cell-derived neurons described defective Parkin recruitment to mitochondria and enhanced mitochondrial biogenesis (Seibler et al., 2011).

PINK1 has been shown to have a diverse catalog of biological functions beyond but not exclusive of mitophagy. PINK1 may play important roles at endoplasmic reticulum (ER) contact sites and in ER stress (Gelmetti et al., 2017; Torres-Odio et al., 2017; Celardo et al., 2016) and also in interactions with MIRO-1, VDAC, Grp78, TRAP1 and mitofusins (McLelland et al., 2018; Kane and Youle, 2011; Grossmann et al., 2019; Geisler et al., 2010; Shoshan-Barmatz et al., 2004). PINK1 has been shown to regulate calcium (Gandhi et al., 2009; Heeman et al., 2011; Soman et al., 2017), iron toxicity (Allen et al., 2013a; Esposito et al., 2013; Horowitz and Greenamyre, 2010; Li et al., 2018), and lipids (Ivatt et al., 2014). Recently PINK1 has been shown to modulate STING-induced inflammation (Sliter et al., 2018) and innate immunity (West et al., 2015; Matheoud et al., 2019; Sliter et al., 2018; Mouton-Liger et al., 2018).

In this study, our aim was to understand the neuronal-specific functions of PINK1 and how this is relevant to Parkinson disease etiology. We differentiated human midbrain specific neurons and showed that PINK1 is not required for maintenance of the mitochondrial networks nor for mitochondrial respiration but rather the fine tuning of mitochondrial matrix metabolism. These alterations may compensate for low mitochondrial quality but ultimately impact neuronal morphogenesis, neurotransmitter homeostasis, and dopamine neuron function.

RESULTS

Homozygous *PINK1* Knockout in Human iPSCs Does Not Inhibit Differentiation of Midbrain-Specific Dopaminergic Neurons (hDANs) but Inhibits Ionophore-Induced Mitophagy

We generated induced pluripotent stem cells (iPSCs) from a healthy female individual that we previously characterized (Reinhardt et al., 2013b) and then introduced a homozygous deletion of *PINK1* using a TALEN directed to Exon 1 (Figure 1A). Twenty-eight to thirty-five days old human midbrain-specific dopaminergic neurons (hDANs) were derived via neural precursor cells (NPCs) using a differentiation protocol we previously described (Reinhardt et al., 2013a). We selected two clonal iPSC lines with no random integration where no *PINK1* transcripts upstream or downstream of the gene edit could be detected (Figure S1A). We stained independent hDAN differentiations for MAP2, a marker of mature neurons, and also, tyrosine hydroxylase (TH), dopamine transporter (DAT), and forkhead box protein A2 (FOXA2), which are markers of mature dopaminergic neurons (Figures S1B and 1B). There are higher amounts of dopaminergic markers TH and DAT for the PINK1 KO lines ($p < 0.0001$). Notably, TH content is significantly more variable in PINK1 KO hDANs ($p = 0.0206$). Gene expression markers TH, MAP2, DAT, FOXA2 were measured alongside markers MAO-A and MAO-B (catecholamine degradation), VGlut1 (glutaminergic neurons), SYP (synaptic marker), and TPH2 (highly expressed in serotonergic neurons). TH and vGlut expression were increased ($p < 0.005$) and TPH2 and MAP2 decreased ($p < 0.005$) in PINK1 KO hDANs compared with their isogenic control (Figure 1C). The proportion of TH-positive neurons in 2D, iPSC-derived hDAN differentiations varies significantly. Because the aim of the protocol is to derive dopaminergic neurons, implicit bias cannot be ruled out during imaging even though counting is blinded. Fully automated procedures and developmental studies *in vivo* will be beneficial. We can conclude that PINK1 KO does not inhibit the differentiation of TH-positive, dopaminergic neurons from NPC intermediates.

Trent University, Nottingham, UK

[11]Interfaculty Institute of Biochemistry, University of Tübingen, Tübingen, Germany

[12]Transversal Translational Medicine, Luxembourg Institute of Health (LIH), Strassen, Luxembourg

[13]Helmholtz Zentrum München, German Research Center for Environmental Health, Institute of Developmental Genetics, Munich-Neuherberg, Germany

[14]These authors contributed equally

[15]Lead Contact

*Correspondence: julia.fitzgerald@uni-tuebingen.de

https://doi.org/10.1016/j.isci.2020.101797

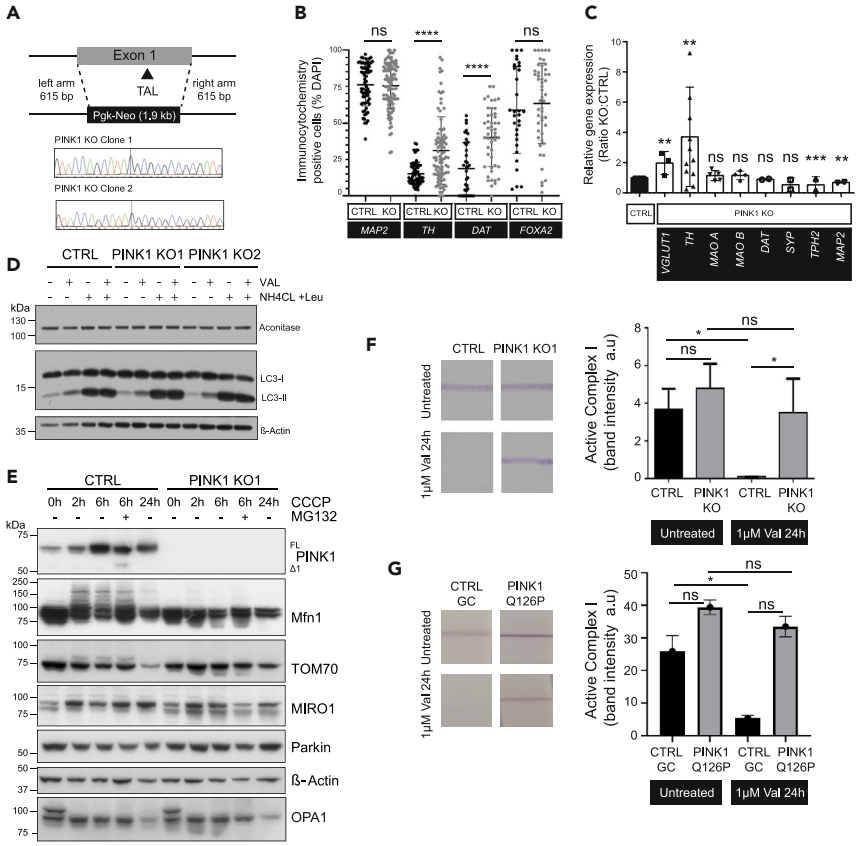

Figure 1. Homozygous *PINK1* Knockout in Human iPSCs Does Not Inhibit Differentiation of hDANs but Inhibits Ionophore-Induced Mitophagy

(A) Scheme showing removal of PINK1 exon 1 (homozygous) using TALEN gene editing in healthy iPSCs. Sequence confirmation of two clonal lines.

(B) Percentage of hDANs in a field of view positive for MAP2, FOXA2, TH, and DAT using immunocytochemistry. Each point on the graph is a technical replicate (nDiff = 4, error bars = SD). ns = not significant, **** = $p < 0.0001$ (Mann Whitney U-test).

(C) Relative gene expression of neuronal markers in PINK1 KO hDANs compared with the healthy control (nDiff = 4, except vGlut, nDiff = 3, error bars = SD). ns = not significant, TH ** = p0.0063 (t test), vGlut ** = p0.0022, TPH2 *** = $p < 0.0002$, MAP2 ** = p0.0043 (all Mann Whitney U-test).

(D) Western blots showing autophagic flux (LC3-II accumulation (C)an LC3-I, mAconitase, and β-actin) in untreated CTRL and PINK1 KO hDANs and those stimulated by Valinomycin (Val, 1µM, 24 h) or NH_4CL (20mM, 4 h) and Leupeptin (Leu, 200µM, 4 h) or both treatments together. nDiff = 3.

(E) Western blots in CTRL and PINK1 KO hDANs untreated or following 10µM CCCP treatment for 0, 2, 6 and 24 h −/+ proteasome inhibition (MG132, 10µM, 6 h). nDiff = 3.

(F) CI dipstick assay for active CI in CTRL and PINK1 KO hDANs treated with or without 1µM Valinomycin for 24 h (left panel). Quantification of dipstick band (nDiff = 3). ns = not significant, * = $p < 0.05$, error bars = SD (t test).

(G) CI dipstick assay for active CI in gene-corrected (GC) CTRL and PINK1 Q126P hDANs treated with or without 1µM valinomycin for 24 h (left panel). Quantification of dipstick band (nDiff = 3). ns = not significant, * = p0.023, error bars = SD (Mann Whitney U-test).

We treated hDANs with the potassium ionophore Valinomycin (Val, 1µM, 24 h) or lysosomal inhibitors (NH_4CL 20mM with Leupeptin (Leu), 200µM for 4 h) and measured autophagic flux using Western blotting for LC3-I/II in combination with mitochondrial aconitase (*m*Aconitase) and β-actin as loading controls. Valinomycin and NH_4Cl induced LC3-II accumulation in control and PINK1 KO hDANs to the same extent (Figure 1D), meaning that PINK1 is dispensable for general autophagy. Neither treatment led to significant depletion of *m*Aconitase (Figure 1D), suggesting that removal of the mitochondrial matrix was not induced under these conditions in hDANs. We then assessed markers of canonical, CCCP ionophore-induced mitophagy in hDANs with the addition of the proteasome inhibitor MG132 at 6 h. PINK1 accumulates in

control hDANs over the CCCP time course peaking at 6 h (Figure 1E) in line with previous work. The ubiquitination and degradation of mitochondrial outer membrane (MOM) proteins Mitofusin1 (Mfn1) and TOM70 was almost absent in PINK1 KO hDANs (Figure 1E), confirming previous work in non-neuronal cells that PINK1 is required for CCCP-induced ubiquitinylation and degradation of Mfn1. The MOM protein and PINK1 substrate MIRO-1 accumulates in all hDAN lines following CCCP treatment (Figure 1E). After 6-h CCCP and proteasomal inhibition MIRO-1 levels were lower in PINK1 KO hDANs (Figure 1E), suggesting that PINK1 could stabilize MIRO-1 during late stages of CCCP-induced mitophagy. Steady state Parkin levels remain unaffected by PINK1 KO (Figure 1E). There was some loss of the OPA-long form and more OPA-short form in CCCP-induced PINK1 KO hDANs consistent with mitochondrial fragmentation at very early stages of mitophagy (Figure 1E).

The potassium ionophore Valinomycin, as CCCP, induces PINK1-Parkin-mediated mitophagy (Rakovic et al., 2019; Zhang et al., 2014a) and was our ionophore of choice to induce mitophagy in hDANs. Because of the 24-h treatment window, it allowed us to optimize a 24-h period of antioxidant withdrawal (removal of potent antioxidants from the neuronal maturation media), which we established for all readouts. In line with previous work in hDANs, ionophores do not induce the turnover of all mitochondrial markers equally. We observe little influence of depolarization on matrix proteins, so we measured the amount of active protein at the inner mitochondrial membrane (IMM) using NADH dehydrogenase (CI). Using PINK1 KO and PINK1 Q126P patient hDAN isogenic lines, we immunoprecipitated CI from fresh lysates and then quantified the conversion of NADH given as a substrate using a simple dipstick assay. We found no significant differences in active CI between the lines under basal conditions (Figures 1F and 1G). Mitophagy induced by Valinomycin depletes active CI in control hDANs after 24 h but not in PINK1 KO nor PINK1 Q126P hDANs (Figures 1F and 1G), suggesting that PINK1-dependent mitophagy (but not PINK1 *per se*) is relevant for complex I activity in hDANs.

PINK1 Knockout hDANs Exhibit Normal Mitochondrial Morphology but Defective ER Calcium Release and Reduced Mitochondrial Membrane Potential

We used electron microscopy (EM) to look for qualitative structural changes to the mitochondria in hDANs devoid of PINK1. EM images from independent hDAN differentiations (PINK KO 1 and PINK KO 2) showed no notable differences in mitochondrial size, shape, or abundance (Figure 2A). Removal of mitochondria following 24-h Valinomycin treatment occurred in control hDANs but not in PINK1 KO hDANs receiving the same treatment (Figure 2A). We observed the presence of round membranous structures in PINK1 KO hDANs, particularly in those treated with the ionophore (indicated by black arrows, Figure 2A). We employed live cell imaging with baculovirus gene transfer into mammalian cells (Bacmam Mito dsRed) on mature hDANs (Figures 2B and S2A) to quantify mitochondrial abundance and morphology. We found no significant differences between PINK1 KO and CTRL hDANs mitochondrial morphology (Figures 2B and S2A). Only PINK1 KO neuronal precursor cells (NPCs) have reduced mitochondrial area per cell compared with isogenic controls (Figure 2B), suggesting mitochondrial fragmentation may be important for neurons to overcome the loss of PINK1 during differentiation. Next, we measured the lifetime (or turnover) of mitochondria using MitoTimer live cell imaging. PINK1 KO causes significantly lower red/green MitoTimer ratio compared with controls, indicating shorter lifespan of the expressed mitochondrial protein and points to mitochondrial renewal in hDANs (Figure S2B). Increased TOM22 fluorescence in flow cytometry (Figure S2C), increased PGC1α levels (Figure S2D), and altered SDHA (nuclear encoded)/MTCO1 (mtDNA encoded) ratio (Figure S2E) support the notion that hDANS lacking PINK1 may employ piecemeal mitochondrial renewal. Statistical significance could only be assigned in the case of PINK1 KO hDANs for the SDHA/MTCO1 mitobiogenesis test after the addition of Valinomycin (Figure S2E).

PINK1 loss of function has previously been associated with calcium toxicity (Gandhi et al., 2009). We measured cytosolic calcium levels using live imaging in PINK1 KO and control following the addition of thapsigargin to release calcium from ER stores. Control hDANs release calcium into the cytosol, which is then buffered. PINK1 KO hDANs respond minimally to thapsigargin stimulation compared with control hDANs (Figure 2C). Response to thapsigargin normalized to the baseline is shown because baseline cytosolic calcium levels were on average higher in control hDANs compared with PINK1 KO (Figure S2F).

Mitochondrial membrane potential ($\Delta\psi$m) is an indicator of mitochondrial function and health. We used the mitochondrial toxin rotenone and FCCP acute treatments to lower the $\Delta\Psi$m further in living cells. We found lower $\Delta\Psi$m in untreated PINK1 KO hDANs compared with controls using flow cytometry (Figure 2D, left

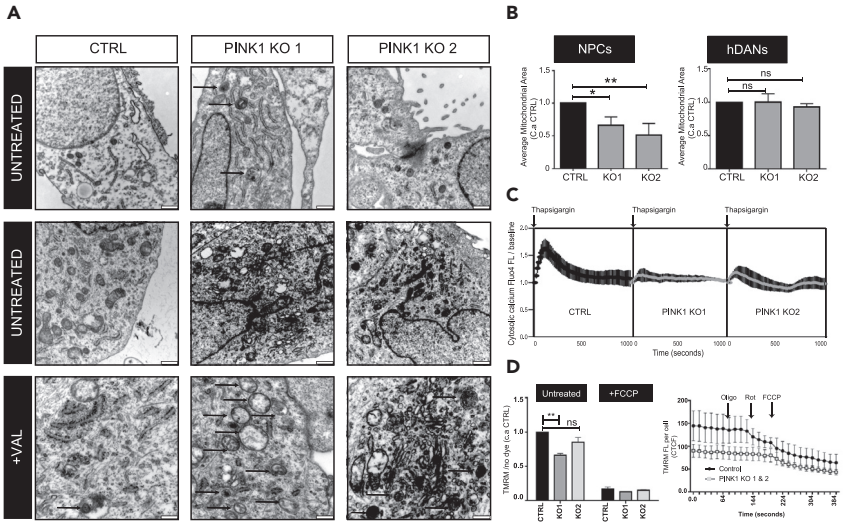

Figure 2. PINK1 Knockout hDANs Exhibit Normal Mitochondrial Morphology but Defective ER Calcium Release and Reduced Mitochondrial Membrane Potential

(A) Electron microscope images of hDANs untreated or treated with valinomycin (Val, 1μM, 24 h). Representative images (nDiff = 3). Black arrows point to membranous structures.

(B) Average mitochondrial area in neuronal progenitor cells (NPCs) and hDANs from live cell imaging (nDiff = 4, error bars = SD). ns = not significant, * = $p < 0.05$, ** = $p < 0.005$ (Mann Whitney U-test).

(C) Cytosolic calcium in response to the addition of thapsigargin during live cell imaging measured by Fluo4 dye fluorescence in hDANs. The total corrected cell fluorescence is shown (nDiff = 4, error bars = SD).

(D) Left panel. Mean average mitochondrial membrane potential ($\Delta\Psi$m) (flow cytometry TMRM fluorescence) for untreated hDANs and those treated acutely with 10μM CCCP (nDiff = 3). Right panel, mean average $\Delta\Psi$m (live cell kinetic imaging, corrected total cell fluorescence, CTCF). Acute treatment with sequential addition of Oligomycin (Oligo), Rotenone (Rot), and FCCP (nDiff = 3, error bars = SD). ** = $p < 0.0026$. ns = not significant (t test).

panel) and live cell imaging (Figure 2D, right panel). Under baseline conditions the $\Delta\Psi$m was reduced by approximately 25%–30% in PINK1 KO hDANs ($p < 0.0001$, endpoint PINK1 KO1 only, and $p < 0.0001$, live imaging corrected total cell fluorescence). Together the pH gradient and the membrane potential constitute an electrochemical proton gradient, which exerts the proton-motive force needed to generate ATP. We show part depolarization in untreated PINK1 KO hDANs, and it is not clear to what extent mitochondrial membrane depolarization is protective and at what point irreversible damage occurs. ATP levels in PINK1 KO hDANs were similar to their control (Figure S2G).

PINK1 KO Impedes *m*Aconitase and Reduces Distinct Metabolite Pools but Does Not Inhibit Respiration in hDANs

Low $\Delta\Psi$m could indicate dysfunctional mitochondrial respiration but basal mitochondrial oxygen consumption was surprisingly elevated over healthy hDANs and respiratory capacity unaffected (Figure 3A). Perhaps one significant observation is that PINK1 KO hDANs are capable of consuming more oxygen than their healthy controls when uncoupled (Figure 3A). Mild uncoupling is used by cells to reduce their oxidative burden. hDANs also prefer glycolysis (indicated by a small increase in extracellular acidification rate, ECAR) when mitochondrial respiration is minimalized (Figure 3A). The substrates pyruvate, glucose, and glutamine are given to the hDANs in the base media before measurement of basal oxygen consumption; therefore, we asked whether mitochondrial substrates could be a limiting factor in PINK1 KO hDANs.

First, we measured the activity of complex I (CI) of the respiratory chain because CI dysfunction has previously been associated with PINK1-Parkinson disease (Morais et al., 2014; Pogson et al., 2014; Vos et al., 2017). Using NADH and coenzyme Q10 as substrates, CI enzyme activity is not significantly affected by loss of PINK1 in hDANs (Figure 3B). We normalize CI activity rates to citrate synthase activity to account for differences in mitochondrial mass and remove any non-CI-specific consumption of NADH by completely inhibiting CI with rotenone in the same set. Because we observed an overall increase (p =

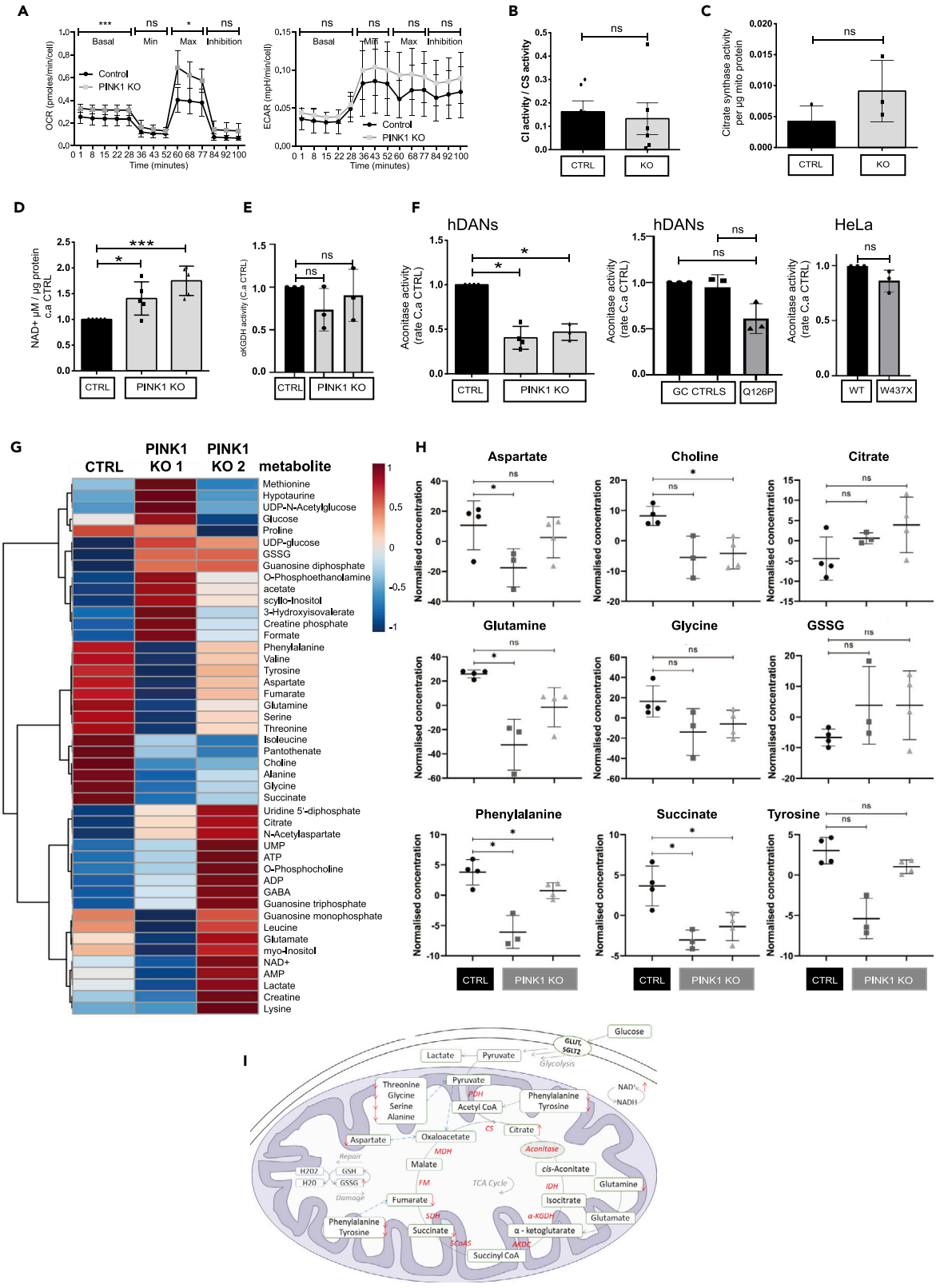
A
B
C
D
E
F
G
H
I
Basal
Min
Max
Inhibition
Control
PINK1 KO
OCR (pmoles/min/cell)
ECAR (mpH/min/cell)
Time (minutes)
CI activity / CS activity
Citrate synthase activity per µg mito protein
CTRL
KO
NAD+ µM / µg protein c.a CTRL
αKGDH activity (C.a CTRL)
Aconitase activity (rate C.a CTRL)
hDANs
HeLa
GC CTRLS
Q126P
WT
W437X
CTRL
PINK1 KO 1
PINK1 KO 2
metabolite
Methionine
Hypotaurine
UDP-N-Acetylglucose
Glucose
Proline
UDP-glucose
GSSG
Guanosine diphosphate
O-Phosphoethanolamine
acetate
scyllo-Inositol
3-Hydroxyisovalerate
Creatine phosphate
Formate
Phenylalanine
Valine
Tyrosine
Aspartate
Fumarate
Glutamine
Serine
Threonine
Isoleucine
Pantothenate
Choline
Alanine
Glycine
Succinate
Uridine 5'-diphosphate
Citrate
N-Acetylaspartate
UMP
ATP
O-Phosphocholine
ADP
GABA
Guanosine triphosphate
Guanosine monophosphate
Leucine
Glutamate
myo-Inositol
NAD+
AMP
Lactate
Creatine
Lysine
Normalised concentration
Aspartate
Choline
Citrate
Glutamine
Glycine
GSSG
Phenylalanine
Succinate
Tyrosine
Glucose
GLUT, SGLT2
Glycolysis
Pyruvate
PDH
Acetyl CoA
CS
Oxaloacetate
MDH
Malate
FM
Fumarate
SDH
Succinate
SCoAS
Succinyl CoA
AKDC
α - ketoglutarate
α-KGDH
Glutamate
IDH
Isocitrate
Aconitase
cis-Aconitate
Glutamine
TCA Cycle
NAD+
NADH
Threonine
Glycine
Serine
Alanine
Phenylalanine
Tyrosine
Aspartate
Repair
Damage
H2O2
H2O
GSH
GSSG

Figure 3. PINK1 KO Impedes *m*Aconitase Activity and Reduces Distinct Amino Acid Pools but Does Not Inhibit Respiration in hDANs

(A) Respiratory analyses of OCR (oxygen consumption rate, left panel) and ECAR (extracellular acidification rate, middle panel) in hDANs. Basal = basal respiration, min = minimal respiration, max = maximal respiration, ns = not significant. *** = p0.0004, * = p0.0158 (nDiff = 4, error bars = SD, t test).

(B) Complex I (CI) enzyme activity normalized to citrate synthase (CS) activity. ns = not significant, (nDiff = 6, error = SD, t test).

(C) Citrate synthase enzyme activity normalized to total protein concentration of the mitochondrial preparation. ns = not significant (nDiff = 3, t test).

(D) NAD^+ concentration of hDANs normalized to total protein and to the healthy control. * = p0.0222, *** = p0.0004. (nDiff = 5, error bars = SD, t test).

(E) Alpha-ketoglutarate dehydrogenase enzyme activity in mitochondrial preparations of PINK1 KO hDANs normalized to µg protein of mitochondria and healthy control. ns = not significant (nDiff = 3, t test).

(F) Aconitase enzyme activity in of PINK1 KO (left panel) and Q126P hDANs (middle panel) with respective controls and wildtype plus W437X HeLa cells (right panel). ns = not significant, * = $p < 0.05$ (nDiff = 3, HeLa n = 3, t test).

(G) A heatmap, generated with MetaboAnalyst, illustrates the Control and PINK KO clone 1 and 2 group relative average metabolite concentration changes. All metabolites were quantified by NMR-based metabolomics. Red indicates high concentrations and blue indicates low concentrations. The metabolites with similar concentration pattern have been grouped together.

(H) NMR metabolomics analysis-based scatterplots were generated for metabolites related to citric acid (TCA, Krebs) cycle and general mitochondria activity. One-way ANOVA & post-hoc tests (Fischer's LSD) were applied to the three-group comparison dataset with adjusted p value (FDR—false discovery rate) cutoff at p0.05. Metabolites tyrosine (p0.0005), phenylalanine (p0.0007), glutamine (p0.0025), and succinate (p0.0042) were reported with the highest significant p values. The t test was applied for individual pair comparison. Where = $p < 0.05$ and ns = not significant.

(I) Mitochondria metabolic pathways illustration focused on the TCA cycle, GSH repair/damage, and NAD+/NADH pool. Red arrows highlight the quantified metabolite concentration changes in PINK1 KO hDANs. Gray arrows indicate the reaction flow; blue long dash arrows show anaplerotic reactions.

0.22 not significant) in citrate synthase enzyme activity (Figure 3C) in PINK1 KO hDANs, we cannot rule out that alterations to mitochondrial dynamics is masking susceptibility to CI function. Nor can we rule out that the availability of substrates to the electron transport chain is an important physiological factor since substrates are given in such assays. Therefore, we looked more closely at wider energy metabolism in PINK1 KO hDANs. The NAD^+ pool was significantly elevated (Figure 3D), suggestive of metabolic compensation or flexibility.

α-ketoglutarate dehydrogenase (αKGDH) is a key, rate-limiting enzyme of the citric acid cycle and a redox sensor. We found no significant alterations to αKGDH activity (Figure 3E). The most notable impact of PINK1 KO was a drastic reduction in the activity of the citric acid cycle enzyme *m*-Aconitase, by around 60% ($p < 0.05$) compared with control hDANs (Figure 3F, left panel). The trend was replicated in PINK1 PD patient hDANs (Q126P) and HeLa PINK1 loss-of-function W437X cells (Figure 3F, middle and right panels). We used a coupled assay for *m*Aconitase that includes the second catalytic step of the reaction requiring iron. mAconitase catalyzes the isomerization of citrate to isocitrate and possesses a 4Fe-4S iron–sulfur cluster. The iron transport protein STEAP3 and the mitochondrial iron transporter Mitoferrin were upregulated in PINK1 KO hDANs (Figure S3A). PINK1 KO hDANs were able to import the radiolabeled proteins ^{35}S-pSU9-DHFR and ^{35}S-Fis1, suggesting relatively normal protein import function into mitochondria (Figure S3B). We recorded no significant levels of cytosolic ROS or changes in reduced glutathione levels in the presence or absence of several stressors (Figure S3C). Citrate or pyruvate transport could also be affected by the mitochondrial proton gradient (Bender and Martinou, 2016).

Nuclear magnetic resonance (NMR) spectroscopy-based metabolomics analysis enabled us to identify a buildup of citrate, which is in-line with reduced *m*Aconitase activity (Figures 3G and 3H). Overall, 46 metabolites from different chemical compound groups and pathways were quantified. We show the average metabolite concentrations in each PINK1 KO and CTRL; however, most of them did not have statistically significant changes (Figure 3G). NMR detected increased levels of oxidized glutathione (GSSG), GDP, and UDP in PINK1 KO hDANs (Figures 3G and 3H).

PINK1 KO hDANs tend to have reduced amino acid pools (shown in the heatmap in Figure 3G), with phenylalanine ($p = 0.0007$, one-way ANOVA), tyrosine ($p = 0.0005$, one-way ANOVA), and glutamine ($p = 0.0025$, one-way ANOVA) having significantly reduced concentrations compared with isogenic control, which has implications for protein synthesis and neurotransmitter metabolism (especially dopamine, which is synthesized from tyrosine).

Reduced glutamine is particularly relevant for antioxidant defense, inflammation, lipid metabolism, and many other metabolic pathways. We also observed significantly reduced succinate levels ($p = 0.0042$, one-way ANOVA), which has implications for mitochondrial respiration and antioxidant status for example. Phenylalanine and succinate were significantly reduced ($p =< 0.016$ and $p =< 0.023$ respectively, using t tests) in PINK1 KO clones compared with control hDANs (Figures 3G, 3H, and S4C).

Principle component analysis (PCA) of the metabolomics data shows that PINK1 KO hDAN clones 1 and 2 vary in metabolic profile (Figure S4A) but sPLSDA suggested distinct group differences (Figures S4B and S4C). Since changes in glutamine levels are associated with neuronal differentiation, we mined the data for the compounds most associated with glutamate (Figure S4D). Here again the phenylalanine and tyrosine were highlighted. PINK1 KO hDANs may utilize succinate and glutamate for energy production. Hormetic dose response to amino acids is known to regulate lifespan and neuronal differentiation and could point toward a compensatory metabolic shift in an attempt to reduce oxidative burden and maintain ATP output. The overall NAD^+ concentration was increased significantly in one PINK1 KO clone, which correlates well with the Figure 3D biochemical assay (Figure S4E). PINK1 KO-induced changes in mitochondrial metabolism are depicted in the diagram in Figure 3I. Whether reduced *m*Aconitase activity is the primary cause of the metabolite changes is still unclear. Glucose, lactate, and pyruvate concentrations were also quantified, yet there were no significant metabolic changes between the control and PINK1 KOs (Figure S4E). Buildup of citrate and a general depletion of metabolites following *m*Aconitase in the citric acid cycle point toward compensatory utilization of amino acids and possibly anaplerotic usage of phenylalanine and tyrosine.

Gene Expression Analysis Highlights the Relevance of PINK1 in Vitamin B6 Salvage and Neuronal-Specific Processes

We hypothesized that the observed metabolic changes due to loss of PINK1 in hDANs could be indirect compensation for reduced mitochondrial quality. We then sought to identify genes relevant to PINK1 in hDANs that could further decipher mechanisms in hDANs. RNAs were deep sequenced in the basal state and following treatment with 1μM Valinomycin (24 h). We compared the top significantly regulated genes ($p < 0.03$) for genotype and treatment. Colored squares show the gene expression as per-row normalized (scaled and centered, i.e. mean = 0, standard deviation = 1) cpm (counts per million) as a measure for gene expression strength (Figure 4A). The raw CPM and Log2FC expression datasets are available as a supplementary Excel file (Table S1). Those significantly regulated genes were used for unbiased pathway analysis using GOrilla (http://cbl-gorilla.cs.technion.ac.il/), a tool for identifying enriched gene ontology (GO) terms. The list of all genes sequenced in the hDANs was used as the background input. The top 15, most significant (ranked by FDR-q-value) GO process terms for the PINK1 KO genotype include tissue development, nervous system development, and cell differentiation (Figure 4B, upper panel graph). For PINK1 KO hDANs challenged with Valinomycin, all GO process significant terms are listed in the table (Figure 4B lower panel, table) and include extracellular structure organization and negative regulation of developmental process. The most significant differentially expressed gene was Pyridoxine-5′-phosphate oxidase (*PNPO*), an enzyme of the vitamin B_6 salvage pathway, important for many cellular functions including amino acid metabolism and neurotransmitter metabolism. *PNPO* gene expression was virtually silenced in PINK1 KO hDANs compared with control. Searching by PNPO-associated pathways, we used Ingenuity software (Qiagen) to find relevant pathways, which included dopamine metabolism. The software plotted all gene expression changes in the dopamine pathway (Figure 4B, bottom right scheme. Red = increased expression and green = decreased expression in PINK1 KO hDANs compared with control). There was a significant and remarkable downregulation of *PNPO* expression ($p < 0.0001$) in both PINK1 KO NPCs and in hDANs (Figure 4C).

Both unbiased metabolite and expression analysis pointed toward PINK1 involvement in dopaminergic differentiation and neuronal-specific regulation. The RNA sequencing analysis for the dopamine synthesis pathway is shown in Figure 4D. We measured the expression of genes involved in dopamine and neurotransmitter metabolism in RNA prepared from the following isogenic models: PINK1 KO hDANs, PINK1 Q126P Parkinson disease patient hDANs (the Q126P mutation is located just after the transmembrane domain of PINK1 (94–110 aa)), HeLa cells gene edited with PINK1 loss-of-function mutation (*PINK1* W437X, kinase domain), three PINK1 Q456X Parkinson disease patient hDAN lines with corresponding gene-corrected controls (*PINK1* Q456X, kinase domain), and PINK1 KO mouse striatum. Statistically significant gene changes occurred for *PNPO* (*PINK1 KO* and *Q456X*), dopa decarboxylase (*Q126P*), and tryptophan hydroxylase 1 (*TPH1, Q126P*) (Figure 4D). TH expression was not significantly different but PINK1 Q126P hDANs were more variable than the gene corrected control (p0.000013). We also measured expression of TPH2 (serotonin biosynthesis), PDXK (pyridoxal kinase, this gene was also unaffected according to RNA sequencing) and DNAJC12 (a co-chaperone together with HSP70 responsible for the proper folding of phenylalanine hydroxylase), which were not significantly altered in any of the PINK1 models. These data confirm reduced PNPO expression occurs in human neurons where PINK1 is

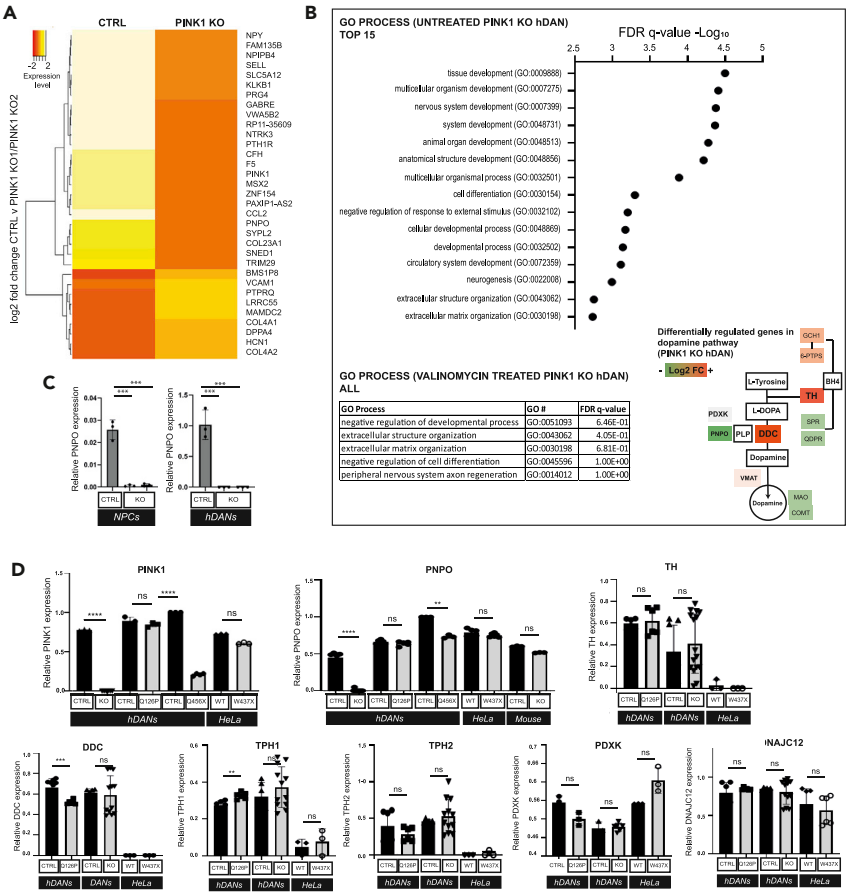

Figure 4. Gene Expression Analysis Highlights the Relevance of PINK1 in Vitamin B6 Salvage and Dopamine Pathways

(A) Deep RNA sequencing revealed disregulated genes. Log2FC of top significant hits ($p < 0.03$) in regard to genotype (PINK1 KO vs control hDANs) or treatment (untreated and 1μM Valinomycin) (n = 3, nDiff = 1), gene expression as per-row normalized (mean = 0, SD = 1) counts per million (cpm).

(B) Pathway analysis of top regulated genes to identify enriched gene ontology (GO) terms with regard to the genotype (upper panel, graph ranked GO terms by significance-FDR q-value) and treatment (10μM Valinomycin, lower left panel, all GO terms listed in table with significance-FDR q-value). Dopamine pathway heatmap of Log2FC gene expression changes in PINK1 KO hDANS compared with control (lower right panel, n = 3, nDiff = 1).

(C) Confirmation of the downregulated *PNPO* expression in PINK1 KO NPCs and hDANs with respective controls by qRT-PCR. *** = $p < 0.0001$ (nDiff = 3, error bars = SD, t test).

(D) qRT-PCR expression analysis of selected genes in the pathway in PINK1 KO, PINK1 Q126P PD hDANs, PINK1 HeLa W437X, and for PNPO PINK1 Q456X PD-derived hDANs (Patient n = 3) and PINK1 KO mouse ventral midbrain (n = 3) with respective isogenic controls. (nDiff = 3, error bars = SD). ns = not significant, PINK1 exon 1–2 (**** = $p < 0.0001$ for PINK1 KO versus CTRL and PINK1 Q456X versus GC CTRL), PNPO (**** = $p < 0.0001$ for PINK1 versus CTRL, ** = p0.0027 for PINK1 Q456X versus GC CTRL), DDC (*** = p0.0010 for PINK1 Q126P versus GC CTRL), TPH1 (** = p0.0035 for Q126P versus GC CTRL). All t test.

significantly depleted. It remains unclear whether depletion of PINK1 or reduced PINK1 kinase function is driving the effect on PNPO.

Combined Proteomic and Transcriptomic Pathway Analyses Highlight Metabolic Role of PINK1

To further identify pathways or interactors that could link PINK1 to neuronal metabolism, we performed quantitative proteomics across independent PINK1 KO hDAN differentiations using crude mitochondrial preparations (Figure S5A). The final assay library contained 3,951 protein IDs including ambiguous hits.

The library contained 3,413 proteins covered by at least one proteotypic peptide. According to MitoCarta2.0 (Calvo et al., 2016), 761 of those proteins were annotated as mitochondrial proteins, which allowed a 65% coverage of the reference mitochondrial proteome. Based on the extracted peptide/protein abundances we calculated the Log2 fold change (Log2FC) values for the control versus PINK1 KO clone 1 and then again for PINK1 KO clone 2 and marked all those proteins that showed significant Log2FC in both PINK1 KO clones. To list the top proteomic hits for PINK1, we removed significant hits between −1.75 and +1.75 to be able to list them in Figure 5A. No other filtering was applied, and the raw mean Log2FC data and list of all significant hits are available as a supplementary Excel file (Table S2). We performed pathway analysis of the top hits against the assay library (Figure 5B). The most significant (FDR-q-value) GO process terms included movement of cell or subcellular components, amide biosynthetic process, cellular amide metabolic process, and peptide biosynthetic process (the top 25 GO process terms are ranked in Figure 5B). These terms point toward PINK1 loss of function in hDAN affecting development and differentiation and metabolism. We overlapped the top regulated genes with top regulated proteins and ranked them by fold change for PINK1 KO. One hundred fourty-four IDs common to both PINK1 KO clones differ from the control (Figure 5C). This list was subjected to pathway analysis against the proteome using Gorilla, and again the top 25 significant GO terms were ranked by FDR-q-value (Figure 5D). Here, core metabolic GO process terms were enriched.

Alternative pathway analysis of proteomic data using Qiagen Ingenuity plotted the interactions between annotated biological pathways (Figure S5D). These data highlight processes relevant to neurons and synapses: androgen signaling, synaptic long-term depression, axonal guidance, CREB signaling, GABA signaling, and EF2 signaling (Figure S5D). The iron sulfur cluster containing calcium-binding protein NECAB2 (also known as MitoNEET) was consistently and significantly more abundant in PINK1 KO hDANs (+2.4 Log2FC, Figure 5A) and was confirmed by Western blotting (Figure S5B). Proteomic data were used to rank disease or function terms and revealed cell migration, severe psychological disorder, and mood disorder for PINK1 KO (Figure S5C).

PINK1 Is Required for Maintenance of Dopamine Pools and Proper Neurotransmitter Uptake in Human Neurons

We next investigated neurotransmitters and dopamine homeostasis in PINK1 hDAN models following data from the unbiased omics approaches. We measured the neurotransmitter content of the hDANs using high-pressure liquid chromatography (HPLC). Short-term and low-dose L-DOPA treatment allows measurement of dopamine (DA) and DA flux accurately. The PINK1 KO hDANs have significantly reduced DOPAC (20-fold reduction, $p < 0.0049$, *n*Diff = 8) and DA levels (6-fold reduction, p0.0026, *n*Diff = 8) (Figure 6A). The ratio of DOPAC/DA was also reduced but not HVA/DA, implicating a role for PINK1 at the presynapse (Figure 6B). We controlled for the number of dopaminergic neurons in the heterogeneous hDAN cultures by monitoring TH at mRNA and protein level in each independent differentiation and HPLC experiment. TH levels vary but not decrease in PINK1 KO hDANs (Figure 6C) HPLC samples, ruling out the possibility that loss of TH positive neurons is responsible for the loss of DA and its metabolites. DA levels inside hDANs and in the media could not be replenished by blocking DA degradation (Figure 6D). Data are not normalized, as hDANs were counted prior to HPLC measurement. Endogenous dopamine is difficult to detect in 2D cultures and requires large hDAN numbers but we measured 0.69 $\pm$ 0.355 ng dopamine per ml in untreated control hDANs (nDiff = 3) and 0.245 $\pm$ 0.122 ng dopamine per ml in untreated PINK1 KO hDANs (KO1 and KO2, nDiff = 4). MAO A and B enzyme activity and MAO-A protein levels were not significantly affected by PINK1 KO (Figure 6H). These data suggest that synthesis or uptake of dopamine, and not degradation, is the major factor contributing to the phenotype. To rule out major oxidation of DA to its Quinone form, which is not detectable by HPLC, we measured total oxidized catecholamines and did not observe any significant differences in the absence or presence of L-DOPA (Figure 6I).

Next, we measured neurotransmitter (NT) uptake by giving a labeled substrate and found it was significantly impaired in PINK1 KO hDANs (Figure 6E). This could not be rescued by inhibition of the monoamine uptake into vesicles (VMAT inhibition), DA synthesis via TH (TH inhibition), or DA degradation (COMT/MAO inhibition) (Figure 6F). This was replicated in PINK1 Q126P hDANs (Figure 6G). Addition of pyridoxal phosphate (PLP) rescue was not feasible because of its ubiquitous inclusion in neuronal base medias. Addition of tetrahydrobiopterin (BH_4) improved NT uptake across all hDAN preparations (Figure 6G). Unlike PLP, which is required for many, diverse biochemical reactions including amino acid conversion, BH_4 is an essential cofactor for aromatic amino acid hydroxylases, alkylglycerol monooxygenase, and nitric oxide

A TOP DIFFERENTIALLY REGULATED PROTEINS (PINK1 KO hDAN)

Protein name	Gene name	Mean Log2FC
Elongation factor 1-alpha 2	EEF1A2	4.192420094
UPF0317 protein C14orf159, mitochondrial	C14orf159	4.157141138
Neurosecretory protein VGF	VGF	3.8658334
Galectin-3	LGALS3	3.25878559
Sulfhydryl oxidase 2	QSOX2	2.878469142
Succinyl-CoA:3-ketoacid coenzyme A transferase 1/2, mitochondrial	OXCT1/2	2.846974378
Carbamoyl-phosphate synthase, mitochondrial	CPS1	2.843917478
Carbonic anhydrase 5B, mitochondrial	CA5B	2.605060207
Succinyl-CoA:3-ketoacid coenzyme A transferase 1, mitochondrial	OXCT1	2.590537888
Junctional adhesion molecule A	F11R	2.584196471
Slit homolog 1 protein	SLIT1	2.469430945
Histone H1.0;Histone H1.0, N-terminally processed	H1F0	2.443224143
N-terminal EF-hand calcium-binding protein 2	NECAB2	2.388285213
Cryptic family protein 1B;Cryptic protein	CFC1;CFC1B	2.34695718
NF-kappa-B inhibitor-interacting Ras-like protein 2	NKIRAS2	2.321456868
Glycine dehydrogenase (decarboxylating), mitochondrial	GLDC	2.211895812
1-phosphatidylinositol 4,5-bisphosphate phosphodiesterase delta-1	PLCD1	2.196720717
Phenylalanine--tRNA ligase, mitochondrial	FARS2	2.134816732
Band 4.1-like protein 5	EPB41L5	2.114930143
Multidrug resistance-associated protein 1	ABCC1	2.079568599
Nicotinate-nucleotide pyrophosphorylase [carboxylating]	QPRT	2.079059777
Mitochondrial fission process protein 1	MTFP1	1.935806295
Pyruvate dehydrogenase (acetyl-transferring)] kinase isozyme 1/2	PDK1;PDK2	1.924509606
Dihydroxyacetone phosphate acyltransferase	GNPAT	1.840879971
Fumarylacetoacetate hydrolase domain-containing protein 2A/2B	FAHD2A/2B	1.837931817
Acyl-coenzyme A thioesterase 13	ACOT13	1.822779947
Armadillo repeat-containing protein 1	ARMC1	1.817550467
Branched-chain-amino-acid aminotransferase, mitochondrial	BCAT2	1.801050485
40S ribosomal protein S24	RPS24	1.77797224

Protein name	Gene name	Mean Log2FC
Major prion protein	PRNP	-1.80624209
Voltage-dependent calcium channel subunit alpha-2/delta-2	CACNA2D2	-1.807879035
T1-TrpRS;T2-TrpRS;Tryptophan--tRNA ligase, cytoplasmic	WARS	-1.901320942
T-complex protein 1 subunit alpha/delta	CCT4;TCP1	-1.904381452
Follistatin-related protein 1	FSTL1	-1.981035678
Calponin-2	CNN2	-1.994760166
ATP-binding cassette sub-family A member 8	ABCA8	-2.004429944
Coronin-1A	CORO1A	-2.059196673
Prenylcysteine oxidase-like	PCYOX1L	-2.064975164
Vasorin	VASN	-2.107535902
Phostensin	PPP1R18	-2.148819609
Polypeptide N-acetylgalactosaminyltransferase 10	GALNT10	-2.154130218
C-type mannose receptor 2	MRC2	-2.16529882
Caldesmon	CALD1	-2.318425112
Gap junction alpha-1 protein	GJA1	-2.39525254
Ephrin type-A receptor 2	EPHA2	-2.405345654
Prolyl 3-hydroxylase 3	LEPREL2	-2.468191654
Myopalladin;Palladin	MYPN;PALLD	-2.631420683
Epidermal growth factor receptor	EGFR	-2.759726181
SPATS2-like protein	SPATS2L	-2.908308718
Heat shock protein beta-1	HSPB1	-2.921190835
Neurofilament light polypeptide	NEFL	-2.959022345
Receptor-type tyrosine-protein phosphatase O	PTPRO	-3.192127725
Actin, alpha/gamma	ACTA1; ACTG2	-3.300479796
Actin, alpha/alpha	ACTA1;ACTA2	-3.471660464
Nucleoside diphosphate kinase, mitochondrial	NME4	-3.509311273
Glypican-4;Secreted glypican-4	GPC4	-3.521926984
Tropomyosin alpha-1 chain;Tropomyosin beta chain	TPM1;TPM2	-3.532751322
Integrin alpha-1	ITGA1	-3.619241666
Collectin-12	COLEC12	-3.756430396
Tropomyosin alpha-1 chain	TPM1	-3.827982433
Collagen alpha-1(XI) chain	COL11A1	-3.872735863
Collagen alpha-1(III) chain	COL3A1	-4.123005226
Myosin regulatory light polypeptide 9	MYL9	-4.515445514
Collagen alpha-1(XII) chain	COL12A1	-4.892665194
Collagen alpha-1(I) chain	COL1A1	-5.803406489

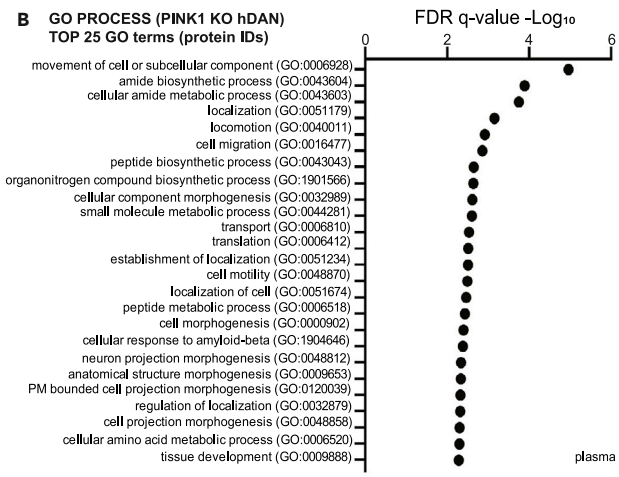

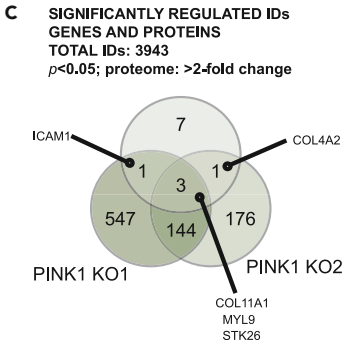

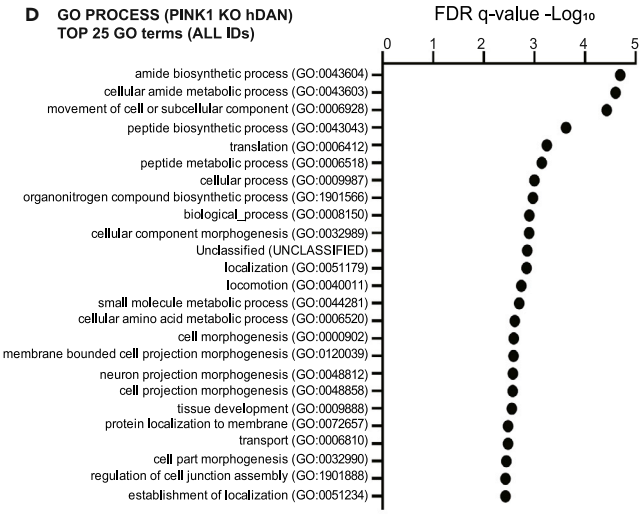

Figure 5. Combined Proteomic and Transcriptomic Pathway Analyses Highlight Metabolic Role of PINK1

(A) Top differentially abundant proteins (mean Log2 fold change), significantly changed in both PINK1 KO1 and PINK1 KO2 hDANs (nDiff = 3, t test).

(B) Unbiased pathway analysis of differentially abundant proteins to generate the top 25 GO process terms for untreated PINK1 KO hDANs (nDiff = 3) based on significance (FDR-q-value).

(C) Overlap of differentially regulated genes and proteins from transcriptomics and proteomics comparing CTRL and PINK1 KO hDANs.

(D) Unbiased pathway analysis of differentially regulated ID (genes and proteins) to generate the top 25 GO process terms for untreated PINK1 KO hDANs based on significance (FDR-q-value).

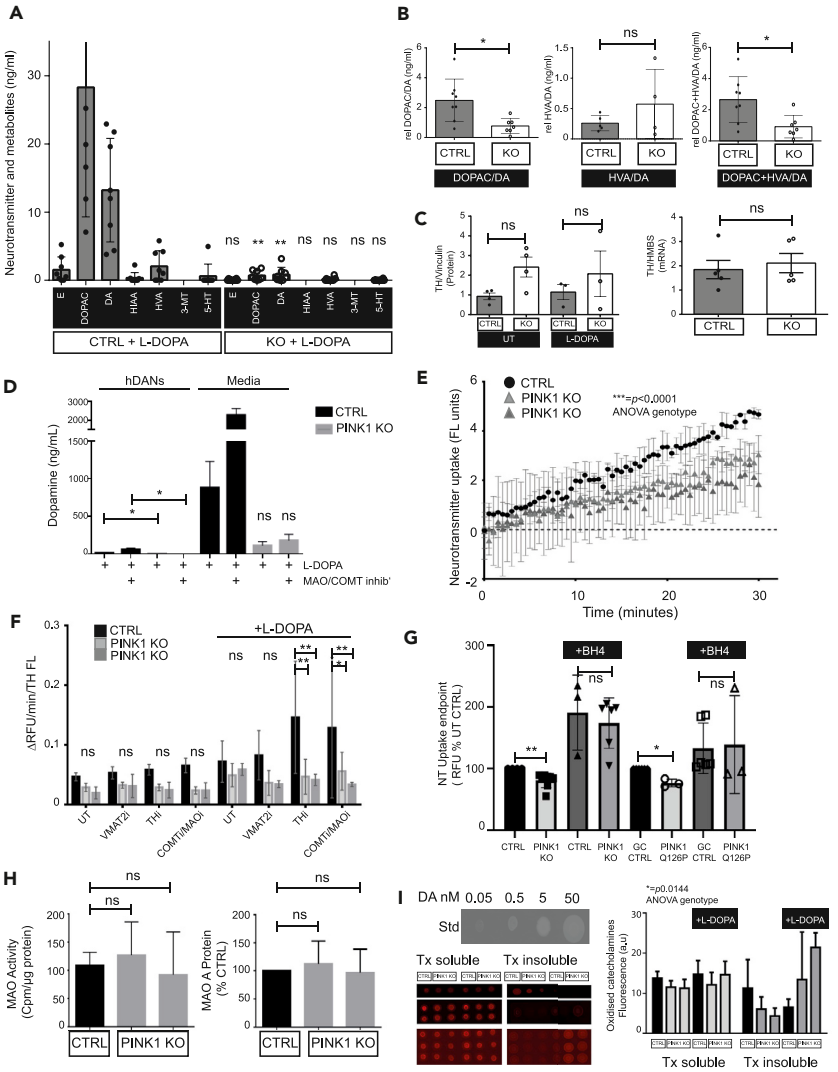

Figure 6. PINK1 Is Required for Maintenance of Dopamine Pools and Proper Neurotransmitter Uptake in Human Neurons

(A) Concentration of neurotransmitters and metabolites epinephrine (E), 3,4-dihydroxyphenylacetic acid (DOPAC), dopamine (DA), 5-hydroxyindoleacetic acid (HIAA), homovanillic acid (HVA), 3-methoxytyramine (3-MT), and 5-hydroxytryptamine/serotonin (5-HT) in hDANs treated with L-DOPA 50µM for 24 h. ** = p0.0045 (DOPAC), p0.0023 (DA), ns = not significant. (nDiff = 8, error bars = SD, t test).

(B) Ratios of DOPAC/DA, HVA/DA, and DOPAC plus HVA/DA. * = p0.0130 (DOPAC/DA), p0.0144 (DOPAC + HVA/DA), ns = not significant (nDiff = 8, error bars = SD, t test).

(C) Tyrosine hydroxylase (TH) protein levels (left panel) and gene expression (right panel) in hDAN aliquots from each HPLC experiments. ns = not significant (nDiff = 4, error bars = SD, t test).

(D) Dopamine concentration in hDANs and in cell culture supernatants treated with L-DOPA for 24 h with or without inhibition of dopamine degradation via COMT and MAOA/B (MOA/COMT inhib'). ** = p0.0036 (L-DOPA, CTRL versus KO), p0.046 (DOPAC + MAOi, CTRL versus KO), ns = not significant (nDiff = 4, error bars = SD, t test).

(E) Neurotransmitter uptake in hDANs measured by the fluorescence of the labeled amine converted inside hDANs only. * = p < 0.0001 (nDiff = 3, error bars = SD, two-way ANOVA).

(F) Quantification of neurotransmitter uptake in hDANs with or without acute inhibition of TH activity (THi), VMAT2 activity (VMAT2i), and COMT and MAOA/B activity (COMTi/MAOi) with or without 24-h 50µM L-DOPA treatment. The rate of uptake is normalized to the amount of TH staining in the well to account for hDAN number. ** = p0.0071 (*L-DOPA + THi, KO1), ** = p0.0048 (*L-DOPA + THi, KO2), * = p0.049 (*L-DOPA + COMTi/MAOi versus KO1), ** = p0.010 (*L-DOPA + COMTi/MAOi vs KO2) (nDiff = 3, t test).

Figure 6. *Continued*

(G) Neurotransmitter uptake in untreated or BH4-treated PINK1 KO and Q126P hDANs with respective isogenic and gene corrected (GC) controls ** = p0.0024 (untreated CTRL versus PINK1 KO), * = p0.023 (untreated GC CTRL versus PINK1 Q126P), ns = not significant. (nDiff = 3, error bars = SD, t test).

(H) MAO A/B activity in hDANs measured by the deamination of a radiolabeled tyramine substrate (left panel) and MAO-A protein levels normalized to GAPDH marker and the healthy control (right panel) ns = not significant (nDiff = 3, error bars = SD, t test).

(I) Catecholamine oxidation in hDANs with or without 50μM L-DOPA treatment for 24 h, showing results for soluble and insoluble fractions. Left panel pictures of blots with oxidized catecholamines. Right panel mean fluorescence signal (a.u.) of oxidized catechols in hDANs (representative blots, nDiff = 3). Two-way ANOVA found significance across the genotypes (* = p0.144), including all the conditions.

synthases and therefore indispensable for the production of catecholamine neurotransmitters including dopamine.

DISCUSSION

Homozygous PINK1 KO causes a significant catecholamine deficit in human mid-brain-specific neurons. The loss of dopamine cannot be attributed to any significant absence of TH-positive neurons in the same hDAN cultures used for catecholamine detection, although TH expression varied across differentiations. Reduced dopamine pools are not a result of increased degradation by monoamine oxidases. Dopamine oxidation remains a possible explanation as we detected increased catecholamine oxidation, but this was inconsistent and in Triton insoluble fractions of PINK1 KO hDANs with L-DOPA treatment. It will be interesting to study whether neuromelanin levels are increased with the advent of mid-brain-specific organoid models. One interesting possibility is that the dopamine deficiency could be caused by mitochondrial metabolism. We show that loss of PINK1-mitochondrial quality control reduces mitochondrial membrane potential and *m*Aconitase activity, yet this is compensated to maintain the mitochondrial networks and meet energy demand. Routing of phenylalanine and tyrosine into the TCA cycle and to acetyl-CoA reduces the pool of precursors for neurotransmitter synthesis. The fact that PINK1 also plays an important role in mitochondrial metabolism in cancer and is highly expressed in non-neuronal brain cells demonstrates that one main function of PINK1 is to help maintain the metabolic quality of mitochondria.

Although PINK1 maintains general mitochondrial quality, it is dispensable for the maintenance of mitochondrial networks and mitochondrial structure in human neurons. This is in line with prior evidence that mitochondrial turnover can occur independently of PINK1 (McWilliams et al., 2018; Lee et al., 2018; Allen et al., 2013a).

Loss of PINK1-mediated, mitochondrial quality control does, however, impair mitochondrial health, seen here by reduced mitochondrial membrane potential. The mitochondrial membrane potential contributes to the proton-motive force needed to generate energy and therefore is seen as a mitochondrial dysfunction. However, the situation might be more complex because mild depolarization and uncoupling has been shown to be beneficial for longevity. Depolarization can trigger stress responses and mitochondrial signaling that are necessary for adaption and reducing oxidative burden. Even small changes to mitochondrial membranes are important for adapting and regulating redox (Vyssokikh et al., 2020) and fueling dopamine release (Graves et al., 2020).

Our data confirm PINK1's role in canonical, ionophore-induced mitophagy while highlighting the relevance of mitochondrial quality control mechanisms that could occur independently of PINK1 (Soubannier et al., 2012; Pickles et al., 2018). Mitochondrial fragmentation occurs in PINK1 KO NPCs but is not observed in the mature hDANs. This supports the model that mitochondrial dynamics can protect healthy mitochondrial domains from elimination when left unchecked by the PINK1-Parkin pathway (Burman et al., 2017; Exner et al., 2007; Ziviani et al., 2010).

Here, we show that PINK1 is dispensable for complex I activity in hDANs. Even in the presence of ionophores, complex I in PINK1 KO hDANs still actively consumes NADH. This observation is in contrast to several studies showing that PINK1 is needed for phosphorylation of complex I (Morais et al., 2014) and reduced complex I activity in PINK1 models and PD patients (Pogson et al., 2014; Flones et al., 2017; Schapira et al., 1989). Our data are obtained from neurons derived from stem cells where the gene knockout has been introduced and therefore does not rule out the possibility that complex I could become impaired

during aging, nor does it take into account the influence of substrate availability, influence of the complete respiratory chain, different states of respiration, lipids, and membrane architecture (Vos et al., 2017). In our study, the depletion of succinate, but not NADH or complex I, points to the relevance of succinate dehydrogenase (complex II) in tuning of respiration and reducing oxidative burden. The mitochondrial matrix protein TRAP1 modulates complex II activity (Sciacovelli et al., 2013) and has previously been shown to act downstream of PINK1 (Fitzgerald et al., 2017; Pridgeon et al., 2007).

PINK1 orchestrates diverse quality control mechanisms (Geisler et al., 2010, Narendra et al., 2010a, Wang et al., 2011a, Sliter et al., 2018, Lai et al., 2015), yet discovery of novel *bonefide* PINK1 substrates in human neurons remains elusive. We show that *m*Aconitase activity and PNPO expression are greatly inhibited by PINK1 KO in neurons. Direct physical interaction between PINK1 and these candidates is unlikely considering their location. The transport of mitochondrial metabolites to the mitochondrial matrix could be a key factor. Other mitochondrial proteins previously described as interactors of PINK1, such as complex I, MIRO-1, or TRAP1, could also be involved in PINK1-metabolic control (Esposito et al., 2013; Morais et al., 2014; Pridgeon et al., 2007; Wang et al., 2011a). The calcium-binding, iron sulfur cluster protein NECAB2 (also known as mitoNEET) and the mitochondrial NDP kinase NME4 identified in this study are interesting candidates for PINK1 interaction.

PINK1 mediates iron homeostasis (Esposito et al., 2013; Kang et al., 2019; Wan et al., 2020; Allen et al., 2013b). The PINK1-PARK2 pathway regulates mitochondrial iron accumulation through affecting SLC25A37 and SCL25A28 degradation, contributing to the abnormal metabolism that supports pancreatic tumor development (Li et al., 2018). Iron is needed for *m*Aconitase activity and must be actively transported into the mitochondrial matrix by mitoferrin, which is upregulated in PINK1 KO hDANs. We propose iron availability in the mitochondrial matrix is responsible for reduced *m*Aconitase activity in PINK1 KO hDANs. Since we do not observe a significant buildup of fumarate nor loss of pyruvate, we can rule out inhibition of *m*Aconitase by succination via fumarate (Ternette et al., 2013). Citrate availability and utilization has been demonstrated for *m*Aconitase role in cancer metabolism. In contrast to certain cancers that permit citrate isomerization at the expense of fatty acid synthesis, PINK1 KO neurons inhibit *m*Aconitase activity, thus promoting fatty acid synthesis. This is important for the mitochondrial and cell membranes and for β-oxidation.

Loss of PINK1 initially induces benign biochemical and metabolic responses and mitochondrial compensation. These biochemical changes are, however, particularly relevant for dopaminergic neurons. Nucleotide and amino acid metabolism were highlighted in metabolomics, transcriptomics, and proteomics experiments in PINK1 KO hDANs. GO terms such as "amide metabolism" describing central metabolic processes ranked the highest when combining the most significant gene and protein changes due to PINK1 KO. Amide metabolism is important in the synthesis of key biochemical intermediates including proteins and lipids and an active component of coenzymes, including CoA.

Amino acids regulate the target of rapamycin (TOR) pathway and are important in aging, inflammation, and neurodegeneration (Auburger et al., 2017; De Simone et al., 2013), reviewed in (Neinast et al., 2019). Phenylalanine and tyrosine, two amino acids reduced in PINK1 KO hDANs, precede tyrosine hydroxylase conversion of tyrosine to L-DOPA, which is the rate-limiting step in the synthesis of dopamine. Dopamine and DOPAC levels are significantly reduced by PINK1 KO in hDANs. Dopamine synthesis also requires pyridoxal phosphate (PLP), the active form of vitamin B6 and a product of the vitamin B6 salvage pathway via PNPO, which is silenced in PINK1 KO hDANs. We suggest that altered dopamine metabolism in PINK1 KO hDANs is due to restriction of its precursors because they are urgently required elsewhere to provide an anaplerotic lifeline to the TCA and support anabolism via acetyl-CoA. The role of PNPO is complex. Silencing of PNPO expression in PINK1 KO NPCs that do not yet express TH or other dopaminergic markers suggests this is tied to the early mitochondrial compensation events resulting from loss of PINK1. Loss of PINK1 expression or kinase function is required for reduced PNPO expression because the PINK1 Q126P point mutation has no effect. High PLP levels can shut down PNPO expression in negative feedback loop, and it is possible that there is an inverse correlation between PINK1 levels and PLP. High PLP levels might be needed for feeding the TCA cycle with amino acid catabolites generated via transamination reactions. The fact that PINK1 Q126P PD hDANS develop neurotransmitter defects without significant reduction of PNPO expression suggests that PNPO silencing here is a relevant to understanding the mechanism but not the biological cause.

Tetrahydrobiopterin (BH_4) is a crucial cofactor in catecholamine metabolism. Here, BH_4 promotes the uptake of catecholamines into neurons. Rescue of catecholamine uptake in PINK1 KO hDANs by BH_4 shows that the uptake defect is secondary since the uptake assay provides a synthetic, exogenous substrate. Because ferrous iron reduces the BH_3 radical back to BH_4 (Berka et al., 2004), the link between PINK1 and Iron and PINK1 and metabolic cofactors needs further elucidation.

Dopamine degradation by MAO and COMT was not significantly affected by loss of PINK1 (we observed significant fluctuations of MAO abundance at the gene and protein level but it was not consistent). TH levels were also highly fluctuating in PINK1 KO hDANs differentiations. TH cofactor biosynthesis is regulated by BH_4 and phenylalanine. These data point toward steering of phenylalanine and tyrosine toward energy metabolism in the mitochondria away from dopamine synthesis.

Whether PINK1 can directly control dopamine metabolism at the mitochondrial outer membrane and mitochondrial-ER contact sites through phosphorylation is an interesting question but so far there is no biochemical evidence. Until candidates are proven, we must assume that it is the loss of mitochondrial quality control and altered MOM landscape that induces metabolic changes. PINK1 involvement in the transport of iron and fine tuning of mitochondrial membranes can mediate such biochemical changes and the consequences go beyond mitophagy in dopaminergic neurons.

Limitations of the Study

- The lack of reliable antibodies to pull down endogenous PINK1 in hDANs limits the biochemical confirmation of PINK1 interactors. Further work using endogenous gene editing of PINK1 in iPSCs and phospho-targeted proteomics is needed.
- It was not possible to reintroduce wild-type human PINK1 into PINK1 KO hDANs to confirm key finding were due to PINK1 KO. Viral transduction is required and low transfection efficiency in iPSC-derived neurons masks any rescue effects without the ability to sort living cells. Introducing antibiotic resistance is limited by the TALEN.

Resource and Availability

Lead Contact

Julia C. Fitzgerald. Hertie Institute for Clinical Brain Research, University of Tübingen, Otfried Müller Strasse 27, Tübingen, 72,076, Germany. Tel: +497071 2981971. Email: julia.fitzgerald@uni-tuebingen.de.

Materials Availability

Please contact us for more information, information on methods, and if you would like to request any materials.

Data and Code Availability

Full Proteomics and transcriptomics peptide and gene lists are deposited and available online at Mendeley Data: Fitzgerald, Julia C. (2020), "Bus et al. iScience. PINK1 hDANs", Mendeley Data, V1, https://doi.org/10.17632/5xv2kwg2c2.1.

High-quality electron microscopy images and other relevant datasets are available at Mendeley Data or on request.

METHODS

All methods can be found in the accompanying Transparent Methods supplemental file.

SUPPLEMENTAL INFORMATION

Supplemental Information can be found online at https://doi.org/10.1016/j.isci.2020.101797.

ACKNOWLEDGMENTS

We greatly acknowledge funding from the Germany Ministry of Education and Research (BMBF) e:Med Demonstrator project MitoPD (FKZ 031A430A). JCF greatly acknowledges support from The German

Research Council (DFG), Research Training Group (RTG) MOMbrane–GRK 2364, And also, The German Center for Neurodegenerative Diseases (DZNE) and The Michael J Fox Foundation for Parkinson's Research (MJFF-15744).

AU-K is supported by Nottingham Trent University Independent Research Fellowship Scheme (UK). This work was supported by research grants from Fonds National de Recherche de Luxembourg (FNR) within the National Center for Excellence in Research on Parkinson's disease (NCER-PD) and MiRisk project [C17/BM/11676395] for RK and GA. DM and KM also acknowledge DFG-RTG MOMbrane (GRK 2364). DVW acknowledges support from the German Science Foundation within the Collaborative Research Centre (CRC) 870, and the Initiative and Network Fund of the Helmholtz Association within the 'ExNet-0041-Phase2-3 ("SyNergy-HMGU")' project.

We would like to thank the iPS cell facility at the HMGU Munich and Annerose Kurz-Drexler as well as Dr. Florian Giesert for generating the hiPSCs and the respective gene-corrected line derived from patients carrying the PINK1 Q126P mutation. We also thank Christine Klein and Philipp Seibler (University of Lübeck, Germany) who kindly shared the human iPSC lines from PD patients carrying the PINK1 Q456X mutation and Jens Schwamborn and Javier Jarazo (LCSB, University of Luxembourg, Luxembourg) for kindly providing their corresponding gene-corrected controls to prepare RNA. We would like to acknowledge The Werner Siemens Imaging Center (WSIC) and Bernd Pichler for access to the NMR spectroscopy for the metabolomics experiments. We thank students and interns in the Fitzgerald lab (Malina John, Max Mattheuer and Lisa Schwarz) who contributed toward establishing and optimizing methodologies. Also E. Ellen Billett for critical review.

AUTHOR CONTRIBUTIONS

Conceptualization, JCF; Methodology, JCF, CB, BS, CJG, CT, DV-W, DR; Validation, JCF, CB, MZ, AS, GA.; Formal Analysis, JCF, MF, AS, CB, KK, CJG, PF-B, AU-K, JA, LZ, CT; Investigation, JCF, CB, MF, SG, MZ, LS, CB, KK, NC, PF-B, AS, FK, CM, JA, AU-K, LZ, KM, GA, CT; Writing—Original Draft, JCF; Writing—Review & Editing, JCF, SG, PK, AU-K, LZ, CB; Visualization, JCF, PK, SG, CJG, CB, JA, LZ, NC; Funding Acquisition, JCF, CJG, MU, RK, TG. and PK; Resources, TG, MU, NC, CT; Supervision, JCF, TG.

DECLARATION OF INTERESTS

The authors declare no conflict of interest.

Received: February 26, 2020
Revised: August 7, 2020
Accepted: November 10, 2020
Published: December 18, 2020

REFERENCES

Allen, G.F., Toth, R., James, J., and Ganley, I.G. (2013a). Loss of iron triggers PINK1/Parkin-independent mitophagy. EMBO Rep. *14*, 1127–1135.

Allen, G.F., Ullah, Y., Hargreaves, I.P., Land, J.M., and Heales, S.J. (2013b). Dopamine but not l-dopa stimulates neural glutathione metabolism. Potential implications for Parkinson's and other dopamine deficiency states. Neurochem. Int. *62*, 684–694.

Anichtchik, O., Diekmann, H., Fleming, A., Roach, A., Goldsmith, P., and Rubinsztein, D.C. (2008). Loss of PINK1 function affects development and results in neurodegeneration in zebrafish. J. Neurosci. *28*, 8199–8207.

Auburger, G., Sen, N.E., Meierhofer, D., Basak, A.N., and Gitler, A.D. (2017). Efficient prevention of neurodegenerative diseases by depletion of starvation response factor Ataxin-2. Trends Neurosci. *40*, 507–516.

Bender, T., and Martinou, J.C. (2016). The mitochondrial pyruvate carrier in health and disease: to carry or not to carry? Biochim. Biophys. Acta *1863*, 2436–2442.

Berka, V., Yeh, H.C., Gao, D., Kiran, F., and Tsai, A.L. (2004). Redox function of tetrahydrobiopterin and effect of L-arginine on oxygen binding in endothelial nitric oxide synthase. Biochemistry *43*, 13137–13148.

Berthier, A., Navarro, S., Jimenez-Sainz, J., Rogla, I., Ripoll, F., Cervera, J., and Pulido, R. (2011). PINK1 displays tissue-specific subcellular location and regulates apoptosis and cell growth in breast cancer cells. Hum. Pathol. *42*, 75–87.

Birsa, N., Norkett, R., Wauer, T., Mevissen, T.E.T., Wu, H.C., Foltynie, T., Bhatia, K., Hirst, W.D., Komander, D., Plun-Favreau, H., and Kittler, J.T. (2014). Lysine 27 ubiquitination of the mitochondrial transport protein Miro is dependent on serine 65 of the parkin ubiquitin ligase. J. Biol. Chem. *289*, 14569–14582.

Blackinton, J.G., Anvret, A., Beilina, A., Olson, L., Cookson, M.R., and Galter, D. (2007). Expression of PINK1 mRNA in human and rodent brain and in Parkinson's disease. Brain Res. *1184*, 10–16.

Burman, J.L., Pickles, S., Wang, C., Sekine, S., Vargas, J.N.S., Zhang, Z., Youle, A.M., Nezich, C.L., Wu, X., Hammer, J.A., and Youle, R.J. (2017). Mitochondrial fission facilitates the selective mitophagy of protein aggregates. J. Cell Biol. *216*, 3231–3247.

Calvo, S.E., Clauser, K.R., and Mootha, V.K. (2016). MitoCarta2.0: an updated inventory of mammalian mitochondrial proteins. Nucleic Acids Res. *44*, D1251–D1257.

Celardo, I., Costa, A.C., Lehmann, S., Jones, C., Wood, N., Mencacci, N.E., Mallucci, G.R., Loh, S.H., and Martins, L.M. (2016). Mitofusin-mediated ER stress triggers neurodegeneration in pink1/parkin models of Parkinson's disease. Cell Death Dis. *7*, e2271.

Chu, C.T. (2019). Multiple pathways for mitophagy: a neurodegenerative conundrum for Parkinson's disease. Neurosci. Lett. *697*, 66–71.

Clark, I.E., Dodson, M.W., Jiang, C., Cao, J.H., Huh, J.R., Seol, J.H., Yoo, S.J., Hay, B.A., and Guo, M. (2006). Drosophila pink1 is required for mitochondrial function and interacts genetically with parkin. Nature *441*, 1162–1166.

Cummins, N., and Gotz, J. (2018). Shedding light on mitophagy in neurons: what is the evidence for PINK1/Parkin mitophagy in vivo? Cell. Mol. Life Sci. *75*, 1151–1162.

Esposito, G., Vos, M., Vilain, S., Swerts, J., De Sousa Valadas, J., Van Meensel, S., Schaap, O., and Verstreken, P. (2013). Aconitase causes iron toxicity in Drosophila pink1 mutants. PLoS Genet. *9*, e1003478.

Exner, N., Treske, B., Paquet, D., Holmstrom, K., Schiesling, C., Gispert, S., Carballo-Carbajal, I., Berg, D., Hoepken, H.H., Gasser, T., et al. (2007). Loss-of-function of human PINK1 results in mitochondrial pathology and can be rescued by parkin. J. Neurosci. *27*, 12413–12418.

Fitzgerald, J.C., Zimprich, A., Berrio, D.A.C., Schindler, K.M., Maurer, B., Schulte, C., Bus, C., Hauser, A.K., Kubler, M., Lewin, R., et al. (2017). Metformin reverses TRAP1 mutation-associated alterations in mitochondrial function in Parkinson's disease. Brain *140*, 2444–2459.

Flones, I.H., Fernandez-Vizarra, E., Lykouri, M., Brakedal, B., Skeie, G.O., Miletic, H., Lilleng, P.K., Alves, G., Tysnes, O.B., Haugarvoll, K., et al. (2017). Neuronal complex I deficiency occurs throughout the Parkinson's disease brain, but is not associated with neurodegeneration or mitochondrial DNA damage. Acta Neuropathol. *135*, 409–425.

Gandhi, S., and Plun-Favreau, H. (2017). Mutations and mechanism: how PINK1 may contribute to risk of sporadic Parkinson's disease. Brain *140*, 2–5.

Gandhi, S., Wood-Kaczmar, A., Yao, Z., Plun-Favreau, H., Deas, E., Klupsch, K., Downward, J., Latchman, D.S., Tabrizi, S.J., Wood, N.W., et al. (2009). PINK1-associated Parkinson's disease is caused by neuronal vulnerability to calcium-induced cell death. Mol. Cell *33*, 627–638.

Gautier, C.A., Kitada, T., and Shen, J. (2008). Loss of PINK1 causes mitochondrial functional defects and increased sensitivity to oxidative stress. Proc. Natl. Acad. Sci. U S A *105*, 11364–11369.

Gegg, M.E., Cooper, J.M., Chau, K.Y., Rojo, M., Schapira, A.H.V., and Taanman, J.W. (2010). Mitofusin 1 and mitofusin 2 are ubiquitinated in a PINK1/parkin-dependent manner upon induction of mitophagy. Hum. Mol. Genet. *19*, 4861–4870.

Geisler, S., Holmstrom, K.M., Skujat, D., Fiesel, F.C., Rothfuss, O.C., Kahle, P.J., and Springer, W. (2010). PINK1/Parkin-mediated mitophagy is dependent on VDAC1 and p62/SQSTM1. Nat. Cell Biol. *12*, 119–131.

Gelmetti, V., De Rosa, P., Torosantucci, L., Marini, E.S., Romagnoli, A., Di Rienzo, M., Arena, G., Vignone, D., Fimia, G.M., and Valente, E.M. (2017). PINK1 and BECN1 relocalize at mitochondria-associated membranes during mitophagy and promote ER-mitochondria tethering and autophagosome formation. Autophagy *13*, 654–669.

Gispert, S., Ricciardi, F., Kurz, A., Azizov, M., Hoepken, H.H., Becker, D., Voos, W., Leuner, K., Muller, W.E., Kudin, A.P., et al. (2009). Parkinson phenotype in aged PINK1-deficient mice is accompanied by progressive mitochondrial dysfunction in absence of neurodegeneration. PLoS One *4*, e5777.

Graves, S.M., Xie, Z., Stout, K.A., Zampese, E., Burbulla, L.F., Shih, J.C., Kondapalli, J., Patriarchi, T., Tian, L., Brichta, L., et al. (2020). Dopamine metabolism by a monoamine oxidase mitochondrial shuttle activates the electron transport chain. Nat. Neurosci. *23*, 15–20.

Grossmann, D., Berenguer-Escuder, C., Bellet, M.E., Scheibner, D., Bohler, J., Massart, F., Rapaport, D., Skupin, A., Fouquier D'herouel, A., Sharma, M., et al. (2019). Mutations in RHOT1 disrupt endoplasmic reticulum-mitochondria contact sites interfering with calcium homeostasis and mitochondrial dynamics in Parkinson's disease. Antioxid. Redox Signal. *31*, 1213–1234.

Guo, T., Liu, T., Sun, Y., Liu, X., Xiong, R., Li, H., Li, Z., Zhang, Z., Tian, Z., and Tian, Y. (2019). Sonodynamic therapy inhibits palmitate-induced beta cell dysfunction via PINK1/Parkin-dependent mitophagy. Cell Death Dis. *10*, 457.

Heeman, B., Van Den Haute, C., Aelvoet, S.A., Valsecchi, F., Rodenburg, R.J., Reumers, V., Debyser, Z., Callewaert, G., Koopman, W.J., Willems, P.H., and Baekelandt, V. (2011). Depletion of PINK1 affects mitochondrial metabolism, calcium homeostasis and energy maintenance. J. Cell Sci. *124*, 1115–1125.

Horowitz, M.P., and Greenamyre, J.T. (2010). Mitochondrial iron metabolism and its role in neurodegeneration. J. Alzheimers Dis. *20*, S551–S568.

Ivatt, R.M., Sanchez-Martinez, A., Godena, V.K., Brown, S., Ziviani, E., and Whitworth, A.J. (2014). Genome-wide RNAi screen identifies the Parkinson disease GWAS risk locus SREBF1 as a regulator of mitophagy. Proc. Natl. Acad. Sci. U S A *111*, 8494–8499.

Jin, S.M., and Youle, R.J. (2013). The accumulation of misfolded proteins in the mitochondrial matrix is sensed by PINK1 to induce PARK2/Parkin-mediated mitophagy of polarized mitochondria. Autophagy *9*, 1750–1757.

Jin, S.M., Lazarou, M., Wang, C., Kane, L.A., Narendra, D.P., and Youle, R.J. (2010). Mitochondrial membrane potential regulates PINK1 import and proteolytic destabilization by PARL. J. Cell Biol. *191*, 933–942.

Julienne, H., Buhl, E., Leslie, D.S., and Hodge, J.J.L. (2017). Drosophila PINK1 and parkin loss-of-function mutants display a range of non-motor Parkinson's disease phenotypes. Neurobiol. Dis. *104*, 15–23.

Kane, L.A., and Youle, R.J. (2011). PINK1 and Parkin flag Miro to direct mitochondrial traffic. Cell *147*, 721–723.

Kane, L.A., Lazarou, M., Fogel, A.I., Li, Y., Yamano, K., Sarraf, S.A., Banerjee, S., and Youle, R.J. (2014). PINK1 phosphorylates ubiquitin to activate Parkin E3 ubiquitin ligase activity. J. Cell Biol. *205*, 143–153.

Kang, R., Xie, Y., Zeh, H.J., Klionsky, D.J., and Tang, D. (2019). Mitochondrial quality control mediated by PINK1 and PRKN: links to iron metabolism and tumor immunity. Autophagy *15*, 172–173.

Kazlauskaite, A., Kondapalli, C., Gourlay, R., Campbell, D.G., Ritorto, M.S., Hofmann, K., Alessi, D.R., Knebel, A., Trost, M., and Muqit, M.M.K. (2014). Parkin is activated by PINK1-dependent phosphorylation of ubiquitin at Ser(65). Biochem. J. *460*, 127–139.

Kitada, T., Pisani, A., Porter, D.R., Yamaguchi, H., Tscherter, A., Martella, G., Bonsi, P., Zhang, C., Pothos, E.N., and Shen, J. (2007). Impaired dopamine release and synaptic plasticity in the striatum of PINK1-deficient mice. Proc. Natl. Acad. Sci. U S A *104*, 11441–11446.

Klein, C., Grunewald, A., and Hedrich, K. (2006). Early-onset parkinsonism associated with PINK1 mutations: frequency, genotypes, and phenotypes. Neurology *66*, 1129–1130.

Koyano, F., Okatsu, K., Kosako, H., Tamura, Y., Go, E., Kimura, M., Kimura, Y., Tsuchiya, H., Yoshihara, H., Hirokawa, T., et al. (2014). Ubiquitin is phosphorylated by PINK1 to activate parkin. Nature *510*, 162.

Lai, Y.C., Kondapalli, C., Lehneck, R., Procter, J.B., Dill, B.D., Woodroof, H.I., Gourlay, R., Peggie, M., Macartney, T.J., Corti, O., et al. (2015). Phosphoproteomic screening identifies Rab GTPases as novel downstream targets of PINK1. EMBO J. *34*, 2840–2861.

Lazarou, M., Sliter, D.A., Kane, L.A., Sarraf, S.A., Wang, C.X., Burman, J.L., Sideris, D.P., Fogel, A.I., and Youle, R.J. (2015). The ubiquitin kinase PINK1 recruits autophagy receptors to induce mitophagy. Nature *524*, 309.

Lee, J.J., Sanchez-Martinez, A., Zarate, A.M., Beninca, C., Mayor, U., Clague, M.J., and Whitworth, A.J. (2018). Basal mitophagy is widespread in Drosophila but minimally affected by loss of Pink1 or parkin. J. Cell Biol. *217*, 1613–1622.

Li, C., Zhang, Y., Cheng, X., Yuan, H., Zhu, S., Liu, J., Wen, Q., Xie, Y., Liu, J., Kroemer, G., et al. (2018). PINK1 and PARK2 suppress pancreatic tumorigenesis through control of mitochondrial iron-mediated immunometabolism. Dev. Cell *46*, 441–455.e8.

Matheoud, D., Cannon, T., Voisin, A., Penttinen, A.M., Ramet, L., Fahmy, A.M., Ducrot, C., Laplante, A., Bourque, M.J., Zhu, L., et al. (2019). Intestinal infection triggers Parkinson's disease-like symptoms in Pink1(-/-) mice. Nature *571*, 565–569.

Mclelland, G.L., Goiran, T., Yi, W., Dorval, G., Chen, C.X., Lauinger, N.D., Krahn, A.I., Valimehr, S., Rakovic, A., Rouiller, I., et al. (2018). Mfn2 ubiquitination by PINK1/parkin gates the p97-

dependent release of ER from mitochondria to drive mitophagy. Elife *7*, e32866.

Mcwilliams, T.G., Prescott, A.R., Montava-Garriga, L., Ball, G., Singh, F., Barini, E., Muqit, M.M.K., Brooks, S.P., and Ganley, I.G. (2018). Basal mitophagy occurs independently of PINK1 in mouse tissues of high metabolic demand. Cell Metab. *27*, 439–449.e5.

Moisoi, N., Fedele, V., Edwards, J., and Martins, L.M. (2014). Loss of PINK1 enhances neurodegeneration in a mouse model of Parkinson's disease triggered by mitochondrial stress. Neuropharmacology *77*, 350–357.

Morais, V.A., Haddad, D., Craessaerts, K., De Bock, P.J., Swerts, J., Vilain, S., Aerts, L., Overbergh, L., Grunewald, A., Seibler, P., et al. (2014). PINK1 loss-of-function mutations affect mitochondrial complex I activity via NdufA10 ubiquinone uncoupling. Science *344*, 203–207.

Mouton-Liger, F., Rosazza, T., Sepulveda-Diaz, J., Ieang, A., Hassoun, S.M., Claire, E., Mangone, G., Brice, A., Michel, P.P., Corvol, J.C., and Corti, O. (2018). Parkin deficiency modulates NLRP3 inflammasome activation by attenuating an A20-dependent negative feedback loop. Glia *66*, 1736–1751.

Narendra, D., Tanaka, A., Suen, D.F., and Youle, R.J. (2008). Parkin is recruited selectively to impaired mitochondria and promotes their autophagy. J. Cell Biol. *183*, 795–803.

Narendra, D.P., Jin, S.M., Tanaka, A., Suen, D.F., Gautier, C.A., Shen, J., Cookson, M.R., and Youle, R.J. (2010a). PINK1 is selectively stabilized on impaired mitochondria to activate Parkin. Plos Biol. *8*, e1000298.

Narendra, D.P., Kane, L.A., Hauser, D.N., Fearnley, I.M., and Youle, R.J. (2010b). p62/SQSTM1 is required for Parkin-induced mitochondrial clustering but not mitophagy; VDAC1 is dispensable for both. Autophagy *6*, 1090–1106.

Neinast, M., Murashige, D., and Arany, Z. (2019). Branched chain amino acids. Annu. Rev. Physiol. *81*, 139–164.

Okatsu, K., Saisho, K., Shimanuki, M., Nakada, K., Shitara, H., Sou, Y., Kimura, M., Sato, S., Hattori, N., Komatsu, M., et al. (2010). p62/SQSTM1 cooperates with Parkin for perinuclear clustering of depolarized mitochondria. Genes to Cells *15*, 887–900.

Parganlija, D., Klinkenberg, M., Dominguez-Bautista, J., Hetzel, M., Gispert, S., Chimi, M.A., Drose, S., Mai, S., Brandt, U., Auburger, G., and Jendrach, M. (2014). Loss of PINK1 impairs stress-induced autophagy and cell survival. PLoS One *9*, e95288.

Park, J., Lee, S.B., Lee, S., Kim, Y., Song, S., Kim, S., Bae, E., Kim, J., Shong, M., Kim, J.M., and Chung, J. (2006). Mitochondrial dysfunction in Drosophila PINK1 mutants is complemented by parkin. Nature *441*, 1157–1161.

Pickles, S., Vigie, P., and Youle, R.J. (2018). Mitophagy and quality control mechanisms in mitochondrial maintenance. Curr. Biol. *28*, R170–R185.

Pogson, J.H., Ivatt, R.M., Sanchez-Martinez, A., Tufi, R., Wilson, E., Mortiboys, H., and Whitworth, A.J. (2014). The complex I subunit NDUFA10 selectively rescues Drosophila pink1 mutants through a mechanism independent of mitophagy. PLoS Genet. *10*, e1004815.

Pridgeon, J.W., Olzmann, J.A., Chin, L.S., and Li, L. (2007). PINK1 protects against oxidative stress by phosphorylating mitochondrial chaperone TRAP1. PLoS Biol. *5*, e172.

Rakovic, A., Ziegler, J., Martensson, C.U., Prasuhn, J., Shurkewitsch, K., Konig, P., Paulson, H.L., and Klein, C. (2019). PINK1-dependent mitophagy is driven by the UPS and can occur independently of LC3 conversion. Cell Death Differ. *26*, 1428–1441.

Reinhardt, P., Glatza, M., Hemmer, K., Tsytsyura, Y., Thiel, C.S., Hoing, S., Moritz, S., Parga, J.A., Wagner, L., Bruder, J.M., et al. (2013a). Derivation and expansion using only small molecules of human neural progenitors for neurodegenerative disease modeling. PLoS One *8*, e59252.

Reinhardt, P., Schmid, B., Burbulla, L.F., Schondorf, D.C., Wagner, L., Glatza, M., Hoing, S., Hargus, G., Heck, S.A., Dhingra, A., et al. (2013b). Genetic correction of a LRRK2 mutation in human iPSCs links parkinsonian neurodegeneration to ERK-dependent changes in gene expression. Cell Stem Cell *12*, 354–367.

Requejo-Aguilar, R., Lopez-Fabuel, I., Fernandez, E., Martins, L.M., Almeida, A., and Bolanos, J.P. (2014). PINK1 deficiency sustains cell proliferation by reprogramming glucose metabolism through HIF1. Nat. Commun. *5*, 4514.

Schapira, A.H., Cooper, J.M., Dexter, D., Jenner, P., Clark, J.B., and Marsden, C.D. (1989). Mitochondrial complex I deficiency in Parkinson's disease. Lancet *1*, 1269.

Schiesling, C., Kieper, N., Seidel, K., and Kruger, R. (2008). Review: Familial Parkinson's disease–genetics, clinical phenotype and neuropathology in relation to the common sporadic form of the disease. Neuropathol. Appl. Neurobiol. *34*, 255–271.

Sciacovelli, M., Guzzo, G., Morello, V., Frezza, C., Zheng, L., Nannini, N., Calabrese, F., Laudiero, G., Esposito, F., Landriscina, M., Defilippi, P., Bernardi, P., and Rasola, A. (2013). The mitochondrial chaperone TRAP1 promotes neoplastic growth by inhibiting succinate dehydrogenase. Cell Metab. *17*, 988–999.

Seibler, P., Graziotto, J., Jeong, H., Simunovic, F., Klein, C., and Krainc, D. (2011). Mitochondrial Parkin recruitment is impaired in neurons derived from mutant PINK1 induced pluripotent stem cells. J. Neurosci. *31*, 5970–5976.

Shoshan-Barmatz, V., Zalk, R., Gincel, D., and Vardi, N. (2004). Subcellular localization of VDAC in mitochondria and ER in the cerebellum. Biochim. Biophys. Acta *1657*, 105–114.

de Simone, R., Vissicchio, F., Mingarelli, C., De Nuccio, C., Visentin, S., Ajmone-Cat, M.A., and Minghetti, L. (2013). Branched-chain amino acids influence the immune properties of microglial cells and their responsiveness to pro-inflammatory signals. Biochim. Biophys. Acta *1832*, 650–659.

Sliter, D.A., Martinez, J., Hao, L., Chen, X., Sun, N., Fischer, T.D., Burman, J.L., Li, Y., Zhang, Z., Narendra, D.P., et al. (2018). Parkin and PINK1 mitigate STING-induced inflammation. Nature *561*, 258–262.

Soman, S., Keatinge, M., Moein, M., Da Costa, M., Mortiboys, H., Skupin, A., Sugunan, S., Bazala, M., Kuznicki, J., and Bandmann, O. (2017). Inhibition of the mitochondrial calcium uniporter rescues dopaminergic neurons in pink1(-/-) zebrafish. Eur. J. Neurosci. *45*, 528–535.

Soubannier, V., Mclelland, G.L., Zunino, R., Braschi, E., Rippstein, P., Fon, E.A., and Mcbride, H.M. (2012). A vesicular transport pathway shuttles cargo from mitochondria to lysosomes. Curr. Biol. *22*, 135–141.

Steinlechner, S., Stahlberg, J., Volkel, B., Djarmati, A., Hagenah, J., Hiller, A., Hedrich, K., Konig, I., Klein, C., and Lencer, R. (2007). Co-occurrence of affective and schizophrenia spectrum disorders with PINK1 mutations. J. Neurol. Neurosurg. Psychiatry *78*, 532–535.

Ternette, N., Yang, M., Laroyia, M., Kitagawa, M., O'Flaherty, L., Wolhulter, K., Igarashi, K., Saito, K., Kato, K., Fischer, R., Berquand, A., Kessler, B.M., Lappin, T., Frizzell, N., Soga, T., Adam, J., and Pollard, P.J. (2013). Inhibition of mitochondrial aconitase by succination in fumarate hydratase deficiency. Cell Rep *3*, 689–700.

Torres-Odio, S., Key, J., Hoepken, H.H., Canet-Pons, J., Valek, L., Roller, B., Walter, M., Morales-Gordo, B., Meierhofer, D., Harter, P.N., et al. (2017). Progression of pathology in PINK1-deficient mouse brain from splicing via ubiquitination, ER stress, and mitophagy changes to neuroinflammation. J. Neuroinflammation *14*, 154.

Valente, E.M., Abou-Sleiman, P.M., Caputo, V., Muqit, M.M., Harvey, K., Gispert, S., Ali, Z., Del Turco, D., Bentivoglio, A.R., Healy, D.G., et al. (2004). Hereditary early-onset Parkinson's disease caused by mutations in PINK1. Science *304*, 1158–1160.

Villa, E., Proics, E., Rubio-Patino, C., Obba, S., Zunino, B., Bossowski, J.P., Rozier, R.M., Chiche, J., Mondragon, L., Riley, J.S., et al. (2017). Parkin-independent mitophagy controls chemotherapeutic response in cancer cells. Cell Rep. *20*, 2846–2859.

Vives-Bauza, C., Zhou, C., Huang, Y., Cui, M., De Vries, R.L., Kim, J., May, J., Tocilescu, M.A., Liu, W., Ko, H.S., et al. (2010). PINK1-dependent recruitment of Parkin to mitochondria in mitophagy. Proc. Natl. Acad. Sci. U S A *107*, 378–383.

Vos, M., Geens, A., Bohm, C., Deaulmerie, L., Swerts, J., Rossi, M., Craessaerts, K., Leites, E.P., Seibler, P., Rakovic, A., et al. (2017). Cardiolipin promotes electron transport between ubiquinone and complex I to rescue PINK1 deficiency. J. Cell Biol. *216*, 695–708.

Vyssokikh, M.Y., Holtze, S., Averina, O.A., Lyamzaev, K.G., Panteleeva, A.A., Marey, M.V., Zinovkin, R.A., Severin, F.F., Skulachev, M.V., Fasel, N., et al. (2020). Mild depolarization of the inner mitochondrial membrane is a crucial component of an anti-aging program. Proc. Natl. Acad. Sci. U S A *117*, 6491–6501.

Walsh, T.G., Van Den Bosch, M.T.J., Lewis, K.E., Williams, C.M., and Poole, A.W. (2018). Loss of the mitochondrial kinase PINK1 does not alter platelet function. Sci. Rep. *8*, 14377.

Wan, Z., Xu, J., Huang, Y., Zhai, Y., Ma, Z., Zhou, B., and Cao, Z. (2020). Elevating bioavailable iron levels in mitochondria suppresses the defective phenotypes caused by PINK1 loss-of-function in Drosophila melanogaster. Biochem. Biophys. Res. Commun. *532*, 285–291.

Wang, X., Winter, D., Ashrafi, G., Schlehe, J., Wong, Y., Selkoe, D., Rice, S., Steen, J., Lavoie, M., and Schwarz, T. (2011a). PINK1 and parkin Target Miro for phosphorylation and degradation to arrest mitochondrial motility. Mol. Biol. Cell *22*, 893–906.

Wang, X.N., Winter, D., Ashrafi, G., Schlehe, J., Wong, Y.L., Selkoe, D., Rice, S., Steen, J., Lavoie, M.J., and Schwarz, T.L. (2011b). PINK1 and parkin Target Miro for phosphorylation and degradation to arrest mitochondrial motility. Cell *147*, 893–906.

Wang, Y., Tang, C.Y., Cai, J., Chen, G.C., Zhang, D.S., Zhang, Z.H., and Dong, Z. (2018). PINK1/Parkin-mediated mitophagy is activated in cisplatin nephrotoxicity to protect against kidney injury. Cell Death Dis. *9*, 1113.

West, A.P., Khoury-Hanold, W., Staron, M., Tal, M.C., Pineda, C.M., Lang, S.M., Bestwick, M., Duguay, B.A., Raimundo, N., Macduff, D.A., et al. (2015). Mitochondrial DNA stress primes the antiviral innate immune response. Nature *520*, 553–557.

Wong, Y.C., and Holzbaur, E.L. (2014). Optineurin is an autophagy receptor for damaged mitochondria in parkin-mediated mitophagy that is disrupted by an ALS-linked mutation. Proc. Natl. Acad. Sci. U S A *111*, E4439–E4448, https://doi.org/10.1073/pnas.1405752111.

Zhang, C., Lee, S., Peng, Y., Bunker, E., Giaime, E., Shen, J., Zhou, Z., and Liu, X. (2014a). PINK1 triggers autocatalytic activation of Parkin to specify cell fate decisions. Curr. Biol. *24*, 1854–1865.

Zhang, Y., Chen, K., Sloan, S.A., Bennett, M.L., Scholze, A.R., O'keeffe, S., Phatnani, H.P., Guarnieri, P., Caneda, C., Ruderisch, N., et al. (2014b). An RNA-sequencing transcriptome and splicing database of glia, neurons, and vascular cells of the cerebral cortex. J. Neurosci. *34*, 11929–11947.

Ziviani, E., Tao, R.N., and Whitworth, A.J. (2010). Drosophila parkin requires PINK1 for mitochondrial translocation and ubiquitinates mitofusin. Proc. Natl. Acad. Sci. U S A *107*, 5018–5023.

iScience, Volume *23*

Supplemental Information

Human Dopaminergic Neurons Lacking PINK1 Exhibit Disrupted Dopamine Metabolism Related to Vitamin B6 Co-Factors

Christine Bus, Laimdota Zizmare, Marita Feldkaemper, Sven Geisler, Maria Zarani, Anna Schaedler, Franziska Klose, Jakob Admard, Craig J. Mageean, Giuseppe Arena, Petra Fallier-Becker, Aslihan Ugun-Klusek, Klaudia K. Maruszczak, Konstantina Kapolou, Benjamin Schmid, Doron Rapaport, Marius Ueffing, Nicolas Casadei, Rejko Krüger, Thomas Gasser, Daniela M. Vogt Weisenhorn, Philipp J. Kahle, Christoph Trautwein, Christian J. Gloeckner, and Julia C. Fitzgerald

Transparent Methods

Ethics statement and data protection

All procedures were in accordance and approved by the ethical board at The University of Tübingen and according to the international standards defined in the declaration of Helsinki. Human samples were obtained with consent and prior ethical approval at The University of Tübingen and the Hertie Institute for Clinical Brain Research Biobank number 146/2009B01. Medical Faculty of the University of Tübingen (https://www.medizin.uni-tuebingen.de/de/medizinische-fakultaet/ethikkommission).

RAW sequences of RNA and peptides will not be made freely available according to EU and German data protection laws to protect the identity of the healthy donor used as an isogenic control in this study. See data availability below.

Generation of human induced pluripotent stem cells (hiPSCs) and *PINK1* knockout

hiPSCs were cultured in self-made E8 media on Vitronectin (VTN-N, Gibco) coated cell culture dishes. iPSCs from a healthy individual that were previously characterized (Reinhardt et al., 2013) were transfected with a TALEN and a homologous construct for *PINK1* exon1 using an Amaxa Nucleofector II with the Stem cell Nucleofection Kit (both from Lonza). The transfected iPSCs were plated on VTN-N –coated 10cm dishes in E8 medium containing 10 µM ROCK inhibitor Y27632. Homologous recombined iPSC colonies were selected with 250 µg/ml G418 (Biochrome) or 10 µgml-1 Blasticidin (InvivoGen) in the second round of TALEN

transfection and re-plated in 12-well plates. Resistant iPSC colonies were characterized by sequencing, qRT-PCR and Western blot to confirm successful homozygous gene knockout. TALENs were designed with the online tool TAL Effector Nucleotide Targeter 2.0 (Cornell University) and generated using a cloning protocol adapted from (Cermak et al., 2011). The following RVD sequences were used for the TALEN monomers: HD HD NI NH NH NG NH NI NH HD NH NH NH NH HD and NI NH HD NG HD HD NH NG HD HD NG HD HD NH HD. Colony-PCR after the first TALEN reaction was conducted with the primers pCR8_F1 (5'-TTGATGCCTGGCAGTTCCCT-3') and pCR8_R1 (5'-CGAACCGAACAGGCTTATGT-3'). After the second Golden Gate reaction the colony-PCR was performed with the primers TAL_F1 (5'-TTGGCGTCGGCAAACAGTGG-3') and TAL_R2 (5'-GGCGACGAGGTGGTCGTTGG-3').

Generation of *PINK1* Q126P hiPSCs and subsequent gene correction

Human fibroblasts were derived from a skin biopsy of a female PD patient with a *PINK1* Q126P mutation in Tübingen of which the family was previously described (Prestel et al., 2008). Human samples were obtained with consent and prior ethical approval at The University of Tübingen and the Hertie Institute for Clinical Brain Research Biobank. The *PINK1* Q126P 15167 hiPSC line was generated using the CoMIP 4in1 method. Reprogramming and characterization (pluripotency, stability of karyotype, and differentiation potential was performed in the iPSC Core Facility of Helmholz Zentrum München. PINK1 Q126P hiPSCs were gene corrected using pCAG-Cas9 vector (Addgene plasmid 84918) and a donor vector carrying a cassette

flanked by a *PINK1* 5'homology arm containing the g.155732C>A and a 3' homology arm. The hiPSCs and the gene corrected line were kindly provided through collaboration with Daniela M. Vogt Weisenhorn and Wolfgang Wurst (Helmholtz Zentrum München, German Research Center for Environmental Health, Institute of Developmental Genetics, Munich-Neuherberg, Germany) as part of a BMBF MitoPD project.

Derivation of NPCs from iPSCs and differentiation into mature, human, mid-brain specific dopaminergic neurons (hDANs)

Mature hDANs were generated from iPSCs via neural progenitor cells (NPC) intermediates using a protocol adapted from (Reinhardt et al., 2013a). The healthy control line (K7.1) has been previously fully characterized and described (Reinhardt et al., 2013a). Two distinct PINK1 KO iPSC clones devoid of PINK1 transcript were used in this study (PINK1 KO1-Δ8.9 and PINK1 KO2-Δ40.7). Briefly, lPSCs were maintained in E8 medium. For the generation of embryoid bodies (EBs), iPSCs were cultured in '50:50 base medium' (one to one mixture of DMEM Hams F12 (#FG4815 Biochrome/Millipore): Neurobasal® medium (#21103-049 Gibco/Thermo Scientific), 1X Penicillin/Streptomycin (Biochrome/Millipore), 1X GlutaMAX supplement Thermo Scientific), 1X B27 supplement (Gibco/Thermo Scientific) and 1X N2 supplement (Gibco/Thermo)) plus the addition of 10µM SB431542 (Sigma, SB), 1µM dorsomorphin, 3µM CHIR99021 (CHIR, Axon) and 0.5µM pumorphamine (PMA, Alexis) on uncoated 6-well cell culture plates. EBs were then transferred to Matrigel (Corning)-coated 6-well plates in NPC maintenance media ('50:50 base medium' plus the addition of 150µM Ascorbic Acid (AA, Sigma), 3µM CHIR, 0.5µM PMA).

After several passages NPCs were cultivated in NPC priming medium (‘50:50 base medium’ plus the addition of 150µM AA and 3µM CHIR99021). Differentiation of confluent NPCs was initiated by cultivation in a patterning medium for seven days (‘50:50 base medium’ plus the addition of 10ng/mL FGF8 (Peprotech), 1µM PMA, 200µM AA, 20ng/mL BDNF (Peprotech). The differentiating neurons were matured in maturation media (’50:50 base medium’ plus the addition of 10ng/mL BDNF, 10ng/mL GDNF (Peprotech), 1ng/mL TGFß-III (Peprotech), 200µM AA, 500 µM dbcAMP (Applichem) and 10µM DAPT (Sigma).

Removal of antioxidant supplements and apoptosis inhibitors

hDANs require N2 and B27 supplements (GIBCO) and ascorbic acid in their culture media. We also routinely use apoptosis inhibitors for splitting and plating NPCs and hDANs, Prior to all experiments, the maturation medium was replaced 24h before the experiment with ‘N2 medium’ (using 50:50 base media without the B27 supplement or ascorbic acid) to reduce excessive amounts of antioxidants in the media that could quench phenotypes. Also, no apoptosis inhibitors such as APOI/ROCK inhibitor were used after the final plating of the hDANs throughout maturation.

Immunofluorescence staining

Mature hDANs were cultivated on Matrigel-coated glass coverslips and fixed with 4% (w/v) paraformaldehyde (PFA, Sigma) in phosphate buffered saline (PBS) for 15 min at room temperature (RT). Permeabilization with ice-cold, neat methanol for 5 min at

-20°C. After washing with 0.01% (v/v) Tween in PBS (PBS-T), the fixed hDANs were blocked with 5% (v/v) normal goat serum in PBS-T for 1h at RT. Afterwards the cells were washed again and incubated overnight at 4°C with the primary antibody in 2.5% (v/v) serum in PBS-T. On the following day the cells were incubated with the secondary fluorescent antibody (#A32721, #A11070, #A21449, #A11010 all from Molecular probes/Thermo Scientific) for 2h at RT in darkness and nuclei stained with DAPI (Sigma). Coverslips were mounted in mounting medium (Dako) on glass slides. Immunofluorescence was imaged using an AxioVert fluorescence microscope (Zeiss). MAP2 (AbCam ab5392) (n=diff5), TH (AbCam ab112) (n=diff5), FOXA2 (Millipore AB4125) (nDiff 3), DAT (Millipore MAB369) (nDiff3). Statistics Figure 1B**:** Blinded IF images were counted manually (IF positive cell as a percent of total cells in a field of view). All values were listed in Graphpad Prism in columns (nDiff=4). The number of % IF positive values from each field of view are as follows; CTRL MAP2 (68), PINK1 KO clones 1 and 2, MAP2 (98), CTRL FOXA2 (31), PINK1 KO clones 1 and 2 FOXA2 (49), CTRL TH (68), PINK1 KO clones 1 and 2, TH (89), CTRL DAT (37) and PINK1 KO clones 1 and 2, DAT (49). Ten outliers were removed by Graphpad Prism (all from CTRL TH). Significance test; All data sets was tested for normal Gaussian distribution using Graphpad Prism (D'Agostino & Pearson test). FOXA2 data was normally distributed and the Unpaired t-test used (ns = not significant). For the remaining non-normally distributed data, the non-parametric Mann Whitney U-test was used. **** = $p<0.0001$. Levene's test of unequal variance was performed in Excel followed by single ANOVA (TH marker CTRL v PINK1 KO p0.0206).

Quantitative Reverse Transcription PCR (qRT-PCR)

RNA was isolated from mature hDANs (and NPCs) using a RNeasy Mini Kit (QIAGEN), including the on-column DNA digestion step. A one-step qRT-PCR was performed on 0.1-1µg RNA (equalized to the same imput amount) with the QuantiTect SYBR Green RT-PCR Kit (QIAGEN) on a LightCycler®480 (Roche). The relative expression levels were calculated with the $2^{-\Delta}$ method, based on a biological reference and housekeeping genes (GAPDH and HMBS) for normalization. Statistics Figure 1C: All ΔΔCt gene of interest/GAPDH were normalised to the CTRL in each case. All values were listed in Graphpad Prism in columns (nDiff=4, except vGlut nDiff = 3). The number of values; CTRL (12), PINK1 KO clones 1 and 2 vGLUT (3), PINK1 KO clones 1 and 2 TH (12), PINK1 KO clones 1 and 2 MAO-A, (11), PINK1 KO clones 1 and 2, MAO-B (10), PINK1 KO clones 1 and 2, DAT (6), PINK1 KO clones 1 and 2, SYP (6), PINK1 KO clones 1 and 2 THP2 (5) and PINK1 KO clones 1 and 2, MAP2 (6). One outlier was removed by Graphpad Prism (from THP2). Significance test; All data sets were tested for normal Gaussian distribution using Graphpad Prism (D'Agostino & Pearson test). TH (**=p0.0063), MAO-A (ns = not significant) and MAO-B (ns = not significant) data were normally distributed and the unpaired T-test used. For the remaining data normality could not be assigned due to low n, the non-parametric Mann Whitney U-test was used. vGlut (**=p0.0022), TPH2 (*** = p<0.0002), MAP2 (**=p0.0043). Statistics Figure 4C and 4D: All ΔΔCt gene of interest/GAPDH were listed in Graphpad Prism in columns. One column was made for both PINK1 KO clones. The data was not normalized to the control in each PINK1 line (except for PINK1 Q456X where there are 3 patients, the ΔΔCt data is normalized to each corresponding gene corrected control line). No outliers were removed by Graphpad Prism. Significance test; assuming normal distribution with

unequal standard deviation, the student's t test with Welch correction was performed. PINK1 exon 1-2 (****=*p*<0.0001 for PINK1 KO v CTRL and PINK1 Q456X v GC CTRL), PNPO (****=*p*<0.0001 for PINK1 v CTRL, **=*p*0.0027 for PINK1 Q456X v GC CTRL), DDC (***=*p*0.0010 for PINK1 Q126P v GC CTRL), TPH1 (**=*p*0.0035 for Q126P v GC CTRL). All t test comparisons were made for all other CTRL and PINK1 lines individually shown for each gene and were not statistically significant. Then all the ΔΔCt values for each gene were listed in two columns in Graphpad Prism (all CTRL/WT v all PINK1 KO/mutation) and each data set for each gene was tested for Gaussian distribution using the D'Agostino & Pearson test. The student's t test with Welch correction; PINK1 (****p<0.0001), DDC (ns=p0.0773), TPH1 (ns=p0.1055), TPH2 (ns=p0.7855), PDXK (ns=p0.8046), DNAJC12 (ns=p0.8663). The non-parametric Mann Whitney U-test; PNPO (*=p0.0192), TH (ns = p0.53). nDiff=3. Levene's variance test was performed in Excel followed by single ANOVA (TH expression GC v Q126P, p0.0000137).

Primer sequences

DNAJC12 (FW:TCACCCAGACAAGCATCCTGA, RV: TTACCTCTGACAACCCAGTGC); **TPH1** (FW: AACCCATGCTTGCAGAGAGT, RV: GCCACAGGACGGATGGAAAA); **TPH2** (FW: GTGGATGTGGCCATGGGTTA, RV: TGGAGAGCTCCCGGAATACA), **PDXK** (FW: GGGATTTGAGATTGACGCGG, RV: GGGACGTACATCGAGCCTTC); **DDC** (FW:GAGCCAGACACGTTTGAGGA, RV: TAGGCGAAGAAGTAGGGGCT); **PNPO** (hFW: AGTCGAAAAGGAAAAGAGCTG; hRV: GGCGGGAGTGGAAGTAG), (msFW:CTGAACCGTCAGGTGCGTGTGGAAGGC,

msRV:AAGGTGCAAGTCTCTCATACACCCAGTCT); **TH** (FW: TGTCTGAGGAGCCTGAGATTCG; RV: GCTTGTCCTTGGCGTCACTG); **PINK1** (exon 1 FW: GGGTCGAGCGCTGCTGCTGCGCTT; exon 2 FW: TCCGGGGGCCCCTGCCTTCC; exon 4 RV: TTGCTTGGGACCTCTCTTGG); **vGLUT1** (FW: GAGTGGCAGTACGTGTTCCT; RV: TCCATTTCGCTGTCGTCACT); **MAO-A** (FW: GCCCTGTGGTTCTTGTGGTATGT; RV: TGCTCCTCACACCAGTTCTTCTC); **MAO-B** (FW: ACTCGTGTGCCTTTGGGTTCAG; RV: TGCTCCTCACACCAGTTCTTCTC); **DAT** (FW: CAAAAGCTGCTTTCCATGGCACACT; RV: CGGCTCCCACCGAGCATTACACT); **SYP** (FW: CAGGGTGGGGCTTAGAATGG; RV: GTGTGTGTGGTGGGGTGCTT); **MAP2** (FW: CCGTGTGGACCATGGGGCTG; RV: GTCGTCGGGGTGATGCCACG); **CP** (FW:CTTAACAGCACCTGGAAGTG; RV:TTGTGAAGGAGGCATCTGTG); **GCLC** (FW:TGAGCTGGGAGGAAACCAAG; RV: AACATGTATTCCACCTCATCGC); **STEAP3** (FW:TTCAGCTTCGTTCAGTCCTC, RV:AGGCAGGTAGAACTTGTAGC); **SLC7A11** (FW:CTTTCAAGGTGCCACTGTTC, RV: GATAATACGCAGGGACTCCA); **Mitoferrin2** (FW: CCATCGACTGCGTCAAGACC; RV: CAAAATAAAGGGCGTGGGCA).

Autophagy and mitophagy induction

Autophagic flux was induced in mature hDANs using Valinomycin (Val, 1µM, 24h) or NH_4CL (20mM, 4h) and Leupeptin (Leu, 200µM, 4h) nDiff=3. Mitophagy was induced in hDANs using; 10µM CCCP for 2h, 4h, 6h, (6h+ 10µM MG132) and 24h or 1µM Valinomycin for 24h nDiff=3.

SDS-PAGE and Western blotting

All cell lysates were prepared in RIPA buffer (Sodium chloride 150mM, Tris-HCL 50mM, Sodium dodecyl sulfate 0.10% (w/v), Sodium deoxycholate 0.50% (w/v), Triton-X-100 1% (v/v)) containing 1X concentration of phosphatase inhibitor cocktail (Complete, Roche) and phosphatase inhibitor cocktail (PhosSTOP, Roche). Briefly, the lysis buffer was added directly to washed cells in dishes or washed cell pellets and kept at 4 °C. Needles were used to further homogenize the lysates (9 passes 20G, 9 passes 27G) and incubated 30 minutes on ice. Insoluble nuclear material was removed after centrifugation at 14,000 rpm for 10 minutes. Proteins were electrophoresed on self-made acrylamide gels or pre-cast Bis-Tris gels (Thermo Scientific) and transferred to nitrocellulose membranes using the iBlot device (Thermo Scientific), with the exception of very large target proteins or heavily lipidated proteins, in which case wet blotting with PVDF membranes was used. Total protein stain Ponceau (Applichem) was used to assess transfer and loading and the PageRuler plus pre-stained protein ladder (Thermo Scientific) for kDa range. Antibodies against PINK1 (Novus), Mitofusin1 (MFN1, AbCam), TOM70 (Santa Cruz), OPA1 (BD Biosciences), Parkin (Cell Signalling Technology), *m*Aconitase (BD Biosciences), β-Actin (Sigma Aldrich), GAPDH (Invitrogen, Thermo Scientific) Tom20 (Santa Cruz Biotechnology), LC3I/II (Novus), PGC1α (AbCam), MIRO-1 (Sigma Aldrich), OPA1 (Novus Biologicals), TH (Millipore), Vinculin (Sigma-Aldrich), MAO-A (In-house produced monoclonal antibody from Ellen Billett, Nottingham Trent University, UK), NECAB2 (a kind gift from Axel Methner, Johannes Gutenberg University Mainz / Germany) and Mitobiogenesis antibody (containing SDHA, GAPDH and MTCO1, AbCam) were used. Secondary antibodies were purchased

from GE Healthcare (HRP-conjugated) and from LiCOR (α-rabbit and mouse Alexa Fluophor™680, α-rabbit and mouse Alexa Fluophor™800). Fluorescence detection and analysis were performed using a LI-CORE blot scanner and Image Studio™ Lite software. Densitometry from Western blot was performed using the Image J 1.41o software (Wayne Rasband; National Institutes of Health, USA). Representative Western blots are shown. For calculating mitochondrial turnover statistics Figure S2D/E. Densitometry data was normalized and no outliers removed. Assuming normal distribution, the student's t test was assigned and ns=not significant, *=p<0.05. nDiff=3. Levenes test of variance was also performed in Microsoft Excel followed by single ANOVA (Untreated mitobiogenesis, p>0.050, valinomycine treated mitobiogenesis p0.030).

Complex I Dipstick Assay

Active Complex I was pulled down from mature hDAN homogenates using the Complex I Dipstick Assay from AbCam (ab109720) according to the manufacturer's instructions. The dipsticks were immediately scanned and the band densitometry quantified using the Image J 1.41o software (Wayne Rasband; National Institutes of Health, USA). Statistics Figure 1F and G: All densitometries derived from scanning the dipstick (nDiff=3) were listed in Graphpad Prism in columns. There were three values for each data set and therefore the test for Gaussian distribution could not be performed. Assuming non-normality, the Mann Whitney U-test was performed (Figure 1G, *=p0.023, Figure 1F, ns =not significant). Assuming normality, the t test was performed (Figure 1F, *=<0.05). 1-way ANOVA with the Kruskal Wallis test was

performed assuming a possible mixture of distributions (Figure 1F, p0.036 and Figure 1G, p0.0003).

Transmission Electron Microscopy

Mature hDANs were seeded on Matrigel (Corning) coated glass coverslips and cultivated for three days prior to treatment with N2 medium with and without 1 µM Valinomycin for 24 hours. After washing and fixation with 2.5% glutaraldehyde (Science Services, Munich, Germany) in cacodylate buffer (pH7.4; Merck-Millipore, Darmstadt, Germany) overnight at 4°C, cells were washed with cacodylate buffer, post fixed in 1% osmiumtetroxide, dehydrated and embedded in epoxide resin (Araldite, Serva, Heidelberg, Germany) as described previously (Wolburg-Buchholz et al., 2009). Ultrathin sections were performed using a Reichert Ultracut ultramicrotome (Leica, Bensheim, Germany) and were analyzed in an EM 10 electron microscope (Zeiss, Oberkochen, Germany). Images were taken by a digital camera (Tröndle, Germany). Qualitative data, representative images are shown, nDiff=3. The high quality images are available on request.

Mitochondrial Morphology (BacMam Mitogreen)

NPCs and mature hDANs were plated on Matrigel covered glass coverslips, treated with CellLight™ Mitochondria-GFP, BacMam 2.0 (Invitrogen) according to manufacturer's instructions for 24 hours in N2 medium. Mitochondria of transfected neurons were imaged using an LSM-510 confocal microscope (Zeiss). Z-stack images were analysed with ImageJ (Fiji, Rasband, W.S., ImageJ, U. S. National

Institutes of Health, Bethesda, Maryland, USA). Statistics Figure 2B: Blinded Z stack IF images were analyzed using ImageJ software (Rasband, W.S., ImageJ, U. S. National Institutes of Health, Bethesda, Maryland, USA, https://imagej.nih.gov/ij/). All values for mitochondrial area were listed in Excel per cell for each field of view (nDiff=4). The data was normalised to the isogenic control for hDANs and for NPCs. No outliers were removed and distribution analysis (D'Agostino & Pearson test) was not possible because nDiff=4. Significance test; Non-normal distribution was assumed and the non-parametric Mann Whitney U-test was used. Ns = not significant, *=$p<0.05$, **=$p<0.005$. Statistics Figure S2A: Blinded IF images were analyzed using particle analysis with IMARIS software and ImageJ (Fiji) across z stacks.

Mathematical calculations for mitochondrial circularity, aspect ratio (length) and form factor (degree of branching) was performed using ImageJ (Fiji), as follows; briefly, images were converted to 8-bit greyscale, → ‘despeckle’, → ‘convolve’, → ’subtract background’, → ‘create binary’ and ‘adjust threshold’ (the threshold must remain the same for all images). ‘Set measurements’, check Area, Perimeter and Fit ellipse. ‘Analyze particles’; Smallest particle set to 1 pixel, → ‘Show outlines’. Data for each mitochondria is listed and raw data copied in Excel. Mean values for each measurement per image is used. Form factor (or degree of branching is the perimeter squared, divided by (4π x area). The data was set in columns in Graphpad Prism in columns (nDiff=4). No outliers were removed and distribution analysis (D'Agostino & Pearson test) was not possible because n=Diff4. Significance test; Non-normal distribution was assumed and the non-parametric Mann Whitney U-test was used. ns = not significant.

Calcium imaging

Mature hDANs were seeded on Matrigel-coated glass coverslips. Fluo-4 Direct Calcium Reagent (Invitrogen) was added to the cells and incubated for one hour at 37°C and 5% CO2. After washing the cells with growth medium, the 24mm coverslips were transferred into self-made imaging chambers and Fluo-4 reagent diluted in growth medium was added. 3 mM EGTA was added per well 10 minutes prior to imaging. Neurons were imaged on a LSM 510 Confocal microscope (Zeiss) taking a picture every 0.5 sec for 25 minutes. A baseline was recorded for two minutes and then 2 µM Thapsigargin was added. The data analysis was performed using ImageJ (Rasband, W.S., ImageJ, U. S. National Institutes of Health, Bethesda, Maryland, USA, https://imagej.nih.gov/ij/). The corrected total cell fluorescence per cell was determined for 10 neurons per experiment and plotted over time to evaluate the calcium signal. To account for variability in Fluo4 signal between imaging sessions we always normalized the Fluo4 signal to the baseline (average Fluo4 signal before the addition of Thapsigargin). Only PINK1 KO clone 1 passed the D'Agostino & Pearson normality test. Therefore, ordinary two-way ANOVA was used for statistical analysis. The data was statically significant comparing genotype across time (****=p<0.0001*).*

Flow cytometry experiments

Mature hDANs were carefully washed in PBS and then treated with Accumax (PAN Biotech) to remove them from the monolayer, quenched in PBS and centrifuged at

300 g for 5 minutes and then incubated in dye, buffer only or dye plus a control. For mitochondrial membrane potential, 200 nM Tetramethylrhodamine, Ethyl Ester, Perchlorate (TMRE, from Thermo Scientific) in PBS or TMRE plus Carbonyl cyanide-p-trifluoromethoxyphenylhydrazone (CCCP, Sigma Aldrich) 10 µM was used. Cells were measured using a MACSQuant® automated flow cytometer (Mitenyi Biotechnology) according to their mean average fluorescence signal. All mean average fluorescence values were divided by the background fluorescence in the same channel in the same unstained cells to account for auto-fluorescence. Statistics Figure 2D (left panel): Assuming normal distribution, the t test was performed. **= p<0.0026. ns=not significant. nDiff=3.

Live Cell Kinetic Measurement of Mitochondrial Membrane Potential

Cells were seeded in Ibidi® dishes and the media exchanged for HBSS containing 200 nM TMRE stain (Thermo Scientific) for 15 minutes at 37°C with CO_2. The TMRE was removed and replaced with 360 µl Hanks buffer. The cells were imaged using a Zeiss Inverted Confocal microscope at Excitation HeNe1, 543 nm and Emission LP 560 nm and brightfield for 20 × 4s cycles. Followed by the addition of 360 µL (0.25 mg/ml Oligomycin), measured for 20 × 4s cycles, 180 µL (10 µM Rotenone), measured for 20 × 4s cycles and 100 µL (10 µM FCCP) and measured for 20-40 × 4s cycles. Using ImageJ (Rasband, W.S., ImageJ, U. S. National Institutes of Health, Bethesda, Maryland, USA, https://imagej.nih.gov/ij/), each frame was analysed for TMRE fluorescence intensity, mean fluorescence and total area. The corrected total cell fluorescence (CTCF) over time was calculated using the formula: *CTCF = fluorescence intensity - (cell area × mean background fluorescence).* Statistics:

Figure 2D (right panel): $p<0.0001$, 2-way ANOVA (CTCF across genotype and time) for corrected total cell fluorescence from live imaging mean CTRL v PINK1 KO1 and KO2 hDANs. nDiff=3.

ATP Assay

ATP was measured using the ViaLight™ Cell Proliferation BioAssay Kit according to the manufacturer's instructions (Lonza) and normalized to the total protein content in each well. Luminescence was detected using SpectraMax L plate reader (Molecular Devices). Technical replicates =3 in each assay and *n*Diff=4. The mean data from each independent experiment comparing PINK1 KO1 and PINK1 KO2 to control was tested using the Mann Whitney U Test and the differences were not significant.

Mitochondrial turnover using MitoTimer™plasmid

Mitotimer is a fluorescent reporter suitable for the investigation of mitochondrial turnover. Based on oxidation state, the fluorescent protein (dsRed mutant) targeted to the mitochondria shifts its emission spectra from green to red as the protein matures (Hernandez et al., 2013). Approximately 100,000 hDANs were seeded per 24-well well on coated coverslips in maturation medium. Mature hDANs were transfected with pMitoTimer from Zhen Yan (Addgene plasmid # 52659;http://n2t.net/addgene:52659 ; RRID:Addgene_52659) using Fugene HD transfection reagent (Promega) according to manufacturer's instructions. Transfection efficiency ranged from 5-10% of total hDANs in the field of view. The hDANs were fixed 48 h post-transfection with 4% (v/v) PFA in PBS for 10 min RT.

Transfected hDANs were imaged for both green (Ex/Em, 488nm/518nm) and red channels (Ex/Em, 543nm/572nm) using a LSM 510 confocal (Zeiss). Z-Stack pictures were analyzed using IMARIS 8.3.1 (Bitplane). Statistics Figure S2B: Data were normalized to the isogenic control in each case and one outlier was removed. The student's t test was performed. **=*p*0.0043 and *=*p*0.0222. nDiff=3.

Tom22 flow cytometry

The Tom22 content in hDANs was measured using the Inside Stain Kit (Miltenyi Biotec). hDANs cultured on Matrigel (Corning) were pre-treated with N2 buffer 24 h prior to the experiment. Cells were harvested, suspended in PBS containing 0.5% BSA and 2mM EDTA and fixed using the same amount of Inside Fix solution (Miltenyi Biotec). After 20 min of incubation at RT neurons were centrifuged for 5 min at 300 g. The supernatant was removed and after a washing step the cell pellets were suspended in Inside Perm with Tom22-GFP antibody (diluted 1:10) or a mouse IgG control. The samples were incubated for 10 min at RT in darkness. To stop the staining samples were diluted with Inside Perm and centrifuged for 5 min at 300g. The supernatant was discarded, and the pellets were suspended in PBS containing 0.5% BSA and 2mM EDTA. Tom22-GFP fluorescence was measured using a MACSQuant Analyzer flow cytometer. IgG background control fluorescence was subtracted from the obtained Tom22-GFP fluorescence for analysis. Statistics Figure S2C: Data was normalised and no outliers removed. Assuming normal distribution, the t test was assigned and ns=not significant, *=p<0.05. nDiff=3.

Respiratory analyses

For the basic mitochondrial stress test, oxygen consumption rates (OCR) and extracellular acidification rates (ECAR) were measured in mature hDANs using a Seahorse™ XF96 Extracellular Flux Analyzer. Cells were seeded in Matrigel coated Seahorse cell plates 24-48h prior to the experiment. During the experiment, OCR/ECAR is measured before any injection of mitochondrial toxins. This is referred to as the basal state (The base media contains glucose, pyruvate and glutamine). The wells were then injected sequentially with 1µM Oligomycin (Santa Cruz Biotechnology) 'minimal respiration', 5µM FCCP (Santa Cruz Biotechnology) 'maximal respiration', and 1µM Antimycin A (Santa Cruz Biotechnology)/ 1µM Rotenone (Sigma Aldrich) 'mitochondrial inhibition'. Following the respiratory analysis, the media is removed and the cells are fixed with 4% (w/v) PFA containing Hoechst stain (1:10,000) for 5 minutes before washing and imaging for automated cell counting (BD Pathway 855, BD Bioscience). Normalisation was performed by counting the number of cells per well of the plate using a high content imager from BD Biosciences (BD Pathway 855). The cell counting was performed by the Pathway 855 using an in house written macro and the dimensions of the wells (0.358 cm^2). Statistics Figure 3A: For each condition per experiment at least 6 wells are used for technical reproducibility. The mean average OCR/ECAR values for each independent experiment are plotted and the error bars show standard deviation (nDiff=4). The t test was used. ns=not significant. ***=*p*0.0004, *=*p*0.0158.

Crude mitochondrial enrichment

Crude mitochondrial enrichment: Fresh cell pellets on ice were suspended in mitochondrial isolation buffer (10 mM HEPES pH 7.4, 50 mM sucrose, 0.4 M

mannitol, 10 mM KCl, 1 mM EGTA, phosphatase and protease inhibitors (Roche)) and passed through 20G, 27G and 30G needles 8 times to disrupt cells. Note: because of the size of hDANs and large amounts of axonal material, we found needle homogenization in the absence of detergents to yield the best mitochondrial enrichments. Fractionation was then achieved by several centrifugation steps. First, samples were centrifuged for 5 min at 1000 xg at 4°C and the supernatant was saved. The pellet was suspended in 500 µL mitochondrial isolation buffer and passed through a 30G needle 8 times before centrifuging 5 min at 900 g at 4°C. The second supernatant was pooled with the first and centrifuged for 15 min at 9000 g at 4°C. The obtained pellet comprises the mitochondrial fraction.

Complex I and citrate synthase activity

Complex I activity was measured in crude mitochondrial enrichments from hDANs previously described in (Fitzgerald et al., 2017) and based on the method of (Hargreaves et al., 2007). Following isolation of crude mitochondria, a total protein content >0.7mg/mL is required to have enough active mitochondria for each sample replicate in each independent assay which needs to be duplicated for the addition of rotenone as a negative control. Citrate synthase activity was measured on the same sample sets and independent differentiations according to (Hargreaves et al., 2007). The citrate synthase activity is used to normalise complex I activity (to account for mitochondrial mass). To later measure the whether citrate synthase activity alone was significantly altered between the groups citrate synthase activity was measured again, this time measuring the exact input protein per well. Citrate synthase is then expressed as a change in absorbance per min per µg protein. The SpectraMax® M

microplate reader (Molecular Devices) was used. Statistics Figure 3B/C. Outlier tests were performed in Graphpad Prism and no outliers were removed. Distribution analysis (D'Agostino & Pearson test) was not possible. The student's t test was used. ns=not significant. nDiff=6 (CI) and nDiff=3 (CS).

NAD^+ and NADH measurement

Mature hDANs were cultivated in N2 medium 24 h before the experiment. Whole cell NAD^+ and NADH-levels were determined using the NAD/NADH Assay Kit (Fluorometric) from Abcam according to manufacturer's instructions. NADH reaction mixture was incubated for 1 hour and fluorescence (Ex/ Em = 540/ 590 nm) was measured using a SpectraMax® M microplate reader (Molecular Devices). Statistics Figure 3D. Outlier tests were performed in Graphpad Prism and no outliers were removed. Distribution analysis (D'Agostino & Pearson test) was not possible. The student's t test was used. *=*p*0.0222, ***=*p*0.0004. nDiff=5. NADH levels were slightly increased in PINK1 KO hDANs but not significantly (data not shown).

αKetoglutarate dehydrogenase activity assay

Mature hDANs were pretreated with N2 medium for 24 hours prior to the experiment. Mitochondria were extracted using the protocol for crude mitochondrial enrichment. Measurement of alpha-ketoglutarate dehydrogenase activity in mitochondria was performed using the alpha-Ketoglutarate Dehydrogenase Activity Colormetric Assay Kit (Sigma-Aldrich) according to manufacturer's instructions. Absorbance (A_{450}) of the samples was measured in kinetic mode every minute for 1h at 37°C on a

SpectraMax®M microplate reader (Molecular Devices). Statistics Figure 3E. Outlier tests were performed in Graphpad Prism and no outliers were removed. The student's t test was used. ns=not significant. nDiff=3.

Mitochondrial Aconitase activity

*m*Aconitase activity was measured in mature hDANs using a protocol from (Pierik et al., 2009). Briefly, hDANs were washed with PBS and the cell pellet suspended in 200µl TNEGT buffer + protease inhibitors. Then dounced on ice using a loose then a tight fitting glass pestle. The homogenates were centrifuge at high and low speeds with rigorous vortexing inbetween (Pierik et al., 2009). The resulting supernatant is then centrifuged for 10 minutes at 13,000g at 4°C. The resulting supernatant is then protein estimated before being used in the assay. Set up of the assay plate: Per well: 95µl trietholamine buffer, 10µl cis aconititic acid (20mM), 20µl Isocitrate dehydrogenase (4U/ml), 10µl NADP (0.1M) and 40µg hDAN supernatant containing the enzyme. Blank = no cis aconitic acid, no isocitrate dehydrogenase. Read absorbance at 340nm, every 30s for 10 mins. We used a SpectraMax® M microplate reader (Molecular Devices). Statistics Figure 3F: Activity rates are normalised to the healthy control. No outliers were removed. The t test was used. *=p<0.05. ns= not significant. nDiff=3, Hela n=3.

Nuclear magnetic resonance (NMR) based metabolomics

hDAN metabolite extraction: hDAN pellets were collected, washed with PBS buffer and quenched in 400 µL ice-cooled ultrapure methanol. The cell suspensions were

then transferred to 2 mL glass tubes (Covaris Adaptive Focused Acoustics AFA^{TM}) and added to 1000 µL of *tert*-butyl methyl ether (MTBE), well mixed and submitted to AFA ultrasound metabolite extraction protocol (*Covaris* E220 Evolution Woburn, USA). Ultrasonication programme setup: two treatment cycles, 1st: 30s, Peak Power 125.0, Duty Factor 32.0, Cycles/Burst 400, Avg. Power 40.0. 2nd: 30s, Peak Power 100.0, Duty Factor 30.0, Cycles/Burst 800, Avg. Power 30.0. The ultrasonication was carried out in cooled water bath, temperature range 5.0 to 15.0 °C. Each cycle was repeated 5 times per sample, total run time per sample was 5 min. Following extraction, 400 µL of ultrapure water were added to the extraction mixture, thoroughly vortexed and centrifuged at 12'000 g for 10 min for optimum phase separation. After centrifugation, the two phases were manually separated: the top lipid (MTBE) layer was transferred to 2 mL HPLC (High-Performance Liquid Chromatography) glass vials; the bottom aqueous phase was moved to 1.5 mL *Eppendorf* cups. Those were then submitted to another centrifugation step at 30'000 g for 10 min to separate any undissolved cell culture residue. Following centrifugation, the aqueous supernatant was transferred to fresh *Eppendorf* cups and evaporated to dryness by a vacuum concentrator (Thermo Fisher Speedvac XYA). **NMR sample preparation**: Dried metabolite pellets were re-suspended in 45 µL 1M K_2HPO_4 (phosphate) buffer (pH = 7.4, containing NaN_3 and 1mM internal NMR standard TSP), thoroughly mixed and then centrifuged for 5 min with 30'000 g. 40 µL of the supernatant was filled into 1.7mm NMR tubes that are compatible to Bruker auto-sampler. **NMR spectra acquisition**: Metabolomics data were acquired on a 14.10 Tesla (600 MHz) ultra-shielded NMR spectrometer (Avance III HD, Bruker BioSpin, Karlsruhe, Germany) equipped with a 1.7 mm room temperature triple resonance probe (^{1}H, ^{13}C, ^{31}P). Spectra were recorded at 298 K. A quick

simple ZG experiment was performed followed by a 1D NOESY (Nuclear Overhauser Effect Spectroscopy) aiming to optimise offset and shim parameters. A CPMG (Carr-Purcell-Meiboom-Gill) experiment was used to suppress residual background signals from remaining macromolecules in the solution and water (time domain = 64k points, sweep width = 20 ppm, 2024 scans, 4 hours per sample). **NMR data analysis and statistics:** The recorded free induction decays (FIDs) were Fourier-transformed (FT) and NMR spectra were processed by Bruker TopSpin 3.6.1 software (automated baseline correction, phase correction and spectra offset adjustment). Metabolite annotation and quantification was done with ChenomX NMR Suite 8.5 software containing the additional HMDB (Human Metabolome Data Base) library. The MetaboAnalyst 4.0 web server (R-based online analysis tool, www.metaboanalyst.ca) was used for statistics. To make samples and features comparable, all data was normalised by a reference sample (probabilistic quotient normalisation (PQN) to account for dilution effects and scaled by the Pareto scaling method (mean-centred and divided by the square root of the standard deviation of each variable). Statistics Figure 3H, initially one-way ANOVA (analysis of variance) with $p < 0.05$. Then the student's t test was applied to compare metabolite concentrations between the control and each PINK1 KO clone. We used Principal component analysis (PCA), sparse partial least squares discriminant analysis (sPLS-DA), pattern hunter and heatmap tools for data visualisation. Independent biological experiments n=4 and nDiff=2.

Mitochondrial import Assay

Radiolabelled proteins were synthesized in rabbit reticulocyte lysate in the presence of ^{35}S-methionine after in vitro transcription by SP6 polymerase from pGEM4 vector (Promega). Radiolabelled precursor proteins were incubated at either 30°C (pSu9-DHFR) or 4°C (Fis1) in import buffer (250 mM sucrose, 0.25 mg/ml BSA, 80 mM KC1, 5 mM $MgCl_2$, 10 mM MOPS-KOH, 2 mM NADH, 4 mM ATP, pH 7.2) with crude mitochondria isolated from mature hDANs. Non-imported pSu9-DHFR molecules were removed by treatment with proteinase K (PK, 50 µg/ml) for 30 min on ice and then PK was inhibited with 5 mM Phenylmethanesulfonyl fluoride. Membrane integration of Fis1 molecules was confirmed by resistance to alkaline extraction (incubation on ice for 30 min with 0.1 M Na_2CO_3 followed by centrifugation to obtain membrane-embedded proteins in the pellet). Finally, samples were heated at 95°C for 5 min before their analysis by SDS-PAGE and autoradiography. Representative images of four independent experiments are shown. Quantification of band densitometry was performed with the AIDA software (Raytest). No outliers were removed. Error bars show standard deviation between independent experiments. Test for normality were not possible. The student's t test was performed comparing control to PINK1 KO hDANs at multiple time points. ns=not significant. nDiff=4.

Cytosolic ROS

Medium was changed to N2 medium 24 h prior to the experiment. On the following day mature hDANs were incubated with N2 medium or N2 medium containing 10µM Rotenone, 1mM Buthionine sulphoximine (BSO) or 50µM Mn-Tbap (a mitochondrial superoxide dismutase 2 mimic) (for 4h before measurement. 100µM dihydroethidium (DiHET) (Santa Cruz Biotechnology) was added to all wells and emission was

measured at 610nm emission (535nm excitation) (chromatin-bound, oxidized DiHET) was measured every 30 secs for 30 min on a SpectraMax® M microplate reader (Molecular Devices). No outliers were removed. Error bars show standard deviation between independent experiments. Tests for normality were not possible. The student's t test was performed and the data showed no statistically significant differences between control and PINK1 KO hDANs. nDiff=3.

Glutathione assay

Neurons on a 96-well plate were treated with different treatment conditions (untreated N2 medium only, 10µM Rotenone, 1mM BSO, and 10µM Rotenone plus 1mM BSO) in N2 medium 24 h prior to the experiment. Cells were briefly washed with HBSS (Gibco) and incubated with 100µL HBSS containing 50µM Monochlorobimane (Sigma) for 40 minutes @37°C, 5% CO2. Blanks were treated the same way but did not contain cells. After washing with HBSS, cells were imaged with a SpectraMax® M microplate reader (Molecular Devices) (Ex 390nm/Em 478nm) to detect the fluorescent adduct of Monochlorobimane and reduced Glutathione (GSH). Background fluorescence obtained from blanks was subtracted for analysis. No outliers were removed. Error bars show standard deviation between independent experiments. Tests for normality were not possible. The t test was performed and the data showed no statistically significant differences between control and PINK1 KO hDANs. nDiff=3.

RNA sequencing

Approximately 5 million hDANs were lysed in 350ml RTL buffer and homogenized using QIAshredder® homogenizer (Qiagen). RNA isolation was performed using RNeasy Mini Kit (Qiagen). RNA was eluted in 30µl RNase-free water. RNA quality was assessed with an Agilent 2100 Bioanalyzer and the Agilent RNA 6000 Nano kit (Agilent). Samples with very high RNA integrity number (RIN > 9) were selected for library construction. For polyA enrichment, a total of 200ng of total RNA was subjected to polyA enrichment and cDNA libraries were constructed using the resulting mRNA and the Illumina TruSeq Stranded mRNA kit (Illumina). Libraries were sequenced as single reads (65 bp read length) on a HighSeq 2500 (Illumina) with a depth of >22 million reads each. Library preparation and sequencing procedures were performed by the same individual and a design aimed to minimize technical batch effects was chosen. Read quality of raw RNA-seq data in FASTQ files was assessed using QoRTs (v1.2.37) to identify sequencing cycles with low average quality, adaptor contamination, or repetitive sequences from PCR amplification. Reads were aligned using STAR (v2.5.3a) allowing gapped alignments to account for splicing to the Ensembl Homo sapiens GRCh37 reference genome. Alignment quality was analyzed using ngs-bits (v0.1) and visually inspected with the Integrative Genome Viewer (v2.4.19). Normalized read counts for all genes were obtained using subread (v1.5.1) and edgeR (v3.24.3). Transcripts covered with less than 1 count-per-million in at least 5 out of 6 samples were excluded from the analysis leaving >13,000 genes for determining differential expression in each of the pair-wise comparisons between experimental groups. For statistics, we used the ederR statistical framework for the calculations (https://bioconductor.org/packages/release/bioc/html/edgeR.html). In short, the methods models read counts per gene using the negative binomial distribution

(capturing the abundance and variability between replicates). Variability is estimated for each gene and on a global scale. After establishing these models, using a generalized linear model (GLM) coefficients are fitted and each gene is tested individually using quasi-likelihood F-test to yield a significance value (*p* value). **Statistics**: For sample size *n*, we used minimum 3 replicates per group. This experiment is following a 2x2 design with 2 samples (nDiff=2) in Valinomycin treatment groups and nDiff=1 sample in control groups for each genotype. **Pathway Analysis**: The heatmap shows the top significant genes (<0.03 *p*-value) in contrast to untreated PINK1 KO vs. untreated isogenic control. Colored squares show the gene expression as per-row normalized (scaled and centered, i.e. mean=0, standard deviation=1) cpm (counts per million as a measure for gene expression strength) values - not log FC values. CPM data were refined by log2 fold change values (logFC) of PINK1 KO hDANs compared to control hDANs for Ingenuity Pathways Analysis (IPA, QIAGEN). First, twenty genes with the highest and lowest log2 fold change were listed. The gene ontology pathway analysis GOrilla was used to generate *p* values and maps of affected processes according to GO terms.

RNA extraction from PINK1 KO mice brain and PINK1 Q456X PD patient hDANs for *PNPO* expression analysis

RNA was prepared from the striatum of three healthy control mice and three PINK1 knockout mice (homogenized using QIAshredder® homogenizer (Qiagen). RNA isolation was performed using RNeasy Mini Kit (Qiagen)) and kindly provided through collaboration with Daniela Vogt-Weisenhorn and Wolfgang Wurst (Helmholtz

Zentrum München, German Research Center for Environmental Health, Institute of Developmental Genetics, Munich-Neuherberg, Germany).

Human iPSC-derived hDANs from three distinct PD patients carrying the PINK1 Q456X mutation and their corresponding gene-corrected isogenic controls were collected at day 30 of differentiation and subjected to RNA extraction by using the RNeasy mini kit (QIAGEN). Briefly, cells were washed twice in PBS and immediately lysed in RTL buffer supplemented with beta-mercaptoethanol. Lysate homogenization was obtained by using the QIAshredder system (QIAGEN), followed by on-column DNase digestion to remove DNA contamination. RNA was finally eluted in nuclease-free water and purity assessed by Nanodrop (A260/A280 and A260/A230 ratios). The cell models were kindly provided by Christine Klein and Philipp Seibler (University of Lubeck, Germany). Their corresponding gene-corrected controls were generated by Jens Schwamborn and Javier Jarazo (University of Luxembourg, Luxembourg).

Proteomics: Quantitative Hyper Reaction Monitoring (HRM)-based mass spectrometry

For lysis, mitochondrial pellets were suspended in 100 µl 6M urea, 100 mM Ammonium bicarbonate pH 8.0 and incubated for 30 min at 4°C. After clearance, the concertation of each lysate was determined by Bradford and 50µg protein per biological replicate were precipitated by methanol chloroform precipitation and processed as described previously (Gloeckner et al., 2009). Briefly, dried protein precipitates were re-dissolved in 30mM Ammonium bicarbonate pH8.0 supplemented with 0.2% RapiGestTM (Waters) surfactant and reduced/ alkylated by

DTT/ Idoacetamide prior to over-night proteolysis with trypsin (Promega). Proteolysis was followed by hydrolysis of the surfactant by TFA according to the manufacturer's protocol. Prior to MS analysis, samples were pre-cleaned with StageTips. For the final dataset two biological replicates (individual differentiations) have been analyzed in three technical replicates. For the generation of the assay library, three DDA runs per condition and biological replicate were acquired. Vacuum-dried samples were re-dissolved in 0.5% TFA and mixed with 2 µl iRT standard peptide mix (Biognosis). Extracted peptides were subsequently subjected to LC-MS/MS-analysis by a 180 min standard method: Tryptic peptide mixtures were injected automatically and loaded at a flow rate of 30 µl/min in 0.1% trifluoroacetic acid in high performance liquid chromatography (HPLC)-grade water onto a nano trap column (300 µm inner diameter × 5 mm precolumn, packed with Acclaim PepMap100 C18, 5 µm, 100 Å; Thermo Scientific). After 3 min, peptides were eluted and separated on the analytical column (75 µm inner diameter × 25 cm, Acclaim PepMap RSLC C18, 2 µm, 100 Å; Thermo Scientific) by a linear gradient from 2% to 30% of buffer B (80% acetonitrile and 0.08% formic acid in HPLC-grade water) in buffer A (2% acetonitrile and 0.1% formic acid in HPLC-grade water) at a flow rate of 300 nl/min over 147 min. Remaining peptides were eluted by a short gradient from 33% or 30% to 95% buffer B in 5 or 10 min. Eluting peptides were analysed on an Q-Exactive Plus mass spectrometer (Thermo Fisher). The HRM acquisition method was adapted from (Bruderer et al., 2015). To improve the quantification performance, 15 instead of the 19 variable windows have been used covering an MS rage from M/Z 457 to M/Z 914 (457-483, 481-506, 504-531, 529-554, 552-576, 574-600, 598-624, 622-650, 648-676, 674-704, 702-735, 733-771, 769-810, 808-856, 854-914). Each HRM sequence was preceded by a full-scan. MS1 and MS2 spectra were acquired in the profile

mode. MS2 spectra were acquired with a stepped collision energy (10% at 25%). DDA MS2 spectra for the assay library creation were acquired with a TOP10 method and in the centroided mode with a fixed collision energy of 25%.

HRM-workflow and statistical analysis

Assay library. The assay library was created with the trans-proteomic-pipeline (TPP v5.1) following published protocols (Schubert et al., 2015). The Thermo RAW files were converted into the mzXML format using MSConvert (Proteowizard v3.0.10765) with the TPP compatibility switch set. The files were filtered for the 150 most intense peaks to reduce the size of the datasets. Briefly, results from four search engines (Mascot [v.2.5.1], Comet [v.2017.01 rev. 1], Myrimatch [v.2.2.10165] and X!Tandem [v.2013.06.15.1]) with trypsin as enzyme, a peptide tolerance of 20 ppm and 3-Methoxythyramine as fixed modification. Individual searches were performed against the human subset of the Swissprot database (release 2016_05, 20201 entries). The masses of the iRT standard (Escher et al., 2012) and decoys (reversed sequences) were added. The assay library was generated by the published TPP workflow. Remaining decoy sequences were manually removed and protein names were replaced by the Uniprot identifiers and the final library was processed and converted into the PQP format by OpenMS (v. 2.4.0). The final assay library contained shuffled decoy sequences in the same amount as the targets. **OpenSWATH workflow.** The openSWATH analysis was performed as previously described (Rost et al., 2017). Briefly, prior to quantification the HRM RAW files were converted into the mzML format at 64bit precision. The files were processed by the OpenSWATHWorkflow (OpenMS v. 2.4.0; Revision: 103a38b) and subsequently analyzed by pyProphet

(v2.01) performing local, experiment-wide and global-statistics for filtering. Files exported to the legacy tsv format were re-aligned by TRIC (Rost et al., 2017). **MSStats.** The TRIC output was processed with SWATH2stats R package (v.1.12.0) (Blattmann et al., 2016) to generate the MSstats format. The final analysis and group comparison was performed using MSStats R package (v.3.12.3) (Choi et al., 2014). Final tables were generated by Perseus (v.1.6.1.3) (Tyanova et al., 2016) to extend the annotation by gene and protein names. **Data analysis**. Statistical significance for each gene Log2FC for control versus PINK1 KO clone 1 and control versus PINK1 KO clone 2 was assigned by an asterisk *p=<0.05 (*n*Diff=3). Filtering to minimize the top hits list for the figure was achieved by removing all significant proteins in the CTRL v PINK1 comparison that did not appear significant in both PINK1 KO lines. Then a cutoff point of +/- Log2FC 1 to limit only relevant fold changes and then an arbitrary +/-1.7 Log2FC cut off (-1.7 to +1.7 Log2FC was removed) to limit the number of hits shown because of space. Qiagen Ingenuity and GOrilla was used to generate a pathway analysis using the LogFC as metrics. The pathway analysis files are available as supplementary Excel files. For the comparison of the mitoproteome with gene expression, RNASeq data were merged on the SWATH proteomic dataset using the 'matching rows by name' function of Perseus.

Measurement of biogenic amines by HPLC-ED

Mature hDANs were expanded during differentiation into 175cm^2 Matrigel coated flasks. For each HPLC experiment, approximately 2-3 175cm^2 flasks were required. Although endogenous dopamine levels could be detected in hDANs derived from much larger cell volumes, we employed 50µM L-DOPA treatment overnight (16h) to

enhance dopamine metabolism without risk of dopamine toxicity (Allen et al., 2013, Burbulla et al., 2017). Following detachment of hDANs with Accumax, the cell suspensions were washed in PBS and cells counted. PBS was used to normalize the number of cells in the suspension. An aliquot of the normalized suspension was taken for preparation of protein lysate and RNA to determine the relative amount of TH positive cells in each experiment and differentiation for each cell line. Fresh (unfrozen) cell pellets kept on ice were suspended in 350µl of a standard HPLC elution buffer that does not contain detergents (Thermo Scientific). The suspensions were homogenized using 5mm stainless steel beads and the tissue lyser LT (Qiagen) for 4 minutes with 50Hz. The cell homogenate was centrifuged at 14000 g for 10 min and the supernatant was filtered through a 0.2µm nylon membrane. Samples were analyzed for catecholamine and indolamine content by ion-pair reverse phase HPLC with colorimetric detection (Ultimate 3000 LC with electrochemical detection ECD3000RS, Thermo Fischer Scientific, California, USA). A hypersil C18 column was used (150x3 mm, 3 µm) and the system was run with a Test mobile phase containing 10% acetonitrile and 1% phosphate buffer (Thermo Fischer Scientific, California, USA) at a flow rate of 0.4 ml/min at 30 °C. The potential of the first channel was set to +350 mV, the second channel to -250 mV. Epinephrine, Norepinephrine, Dopamine, 3,4-dihydroxyphenylacetic acid (DOPAC), homovanillic acid (HVA), 5-hydroxyindol-acetic acid (HIAA), 3-Methoxytyramine (3-MT) and 5-hydroxytryptamine/serotonin (5-HT), concentration was determined by comparing peak areas of the samples with those of standards using Chromeleon 7 chromatography data system software. The neurochemicals in standards were determined with a high correlation linearity ($r^2 = 0.98$) and good reproducibility in retention time (0.03%). The limit of detection was <1 pg on column for all the

metabolites analyzed. Statistics Figure 6A: The data was not normalized. One outlier for dopamine was removed from the control hDAN dataset. The data was normally distributed. The Student's t test was performed, **=*p*0.0045 (DOPAC), *p*0.0023 (DA), ns=not significant. nDiff=8. Figure 6B: The data was not normalized. One outlier for dopamine was removed from the control hDAN dataset. The data was normally distributed. The Student's t test was performed, *=*p*0.0130 (DOPAC/DA), *p*0.0144 (DOPAC+HVA/DA), ns=not significant. nDiff=8. Figure 6C: The Student's t test was performed, ns=not significant. nDiff=3. Figure 6D: The data was not normalized. No outliers were removed. Data distribution analysis was not possible. The Student's t test was performed, **=*p*0.0036 (L-DOPA, CTRL v KO), *p*0.046 (DOPAC+MAOi, CTRL v KO), ns=not significant. nDiff=4.

Neurotransmitter Uptake Assay

Neurotransmitter transporter activity in hDANs was measured using the Neurotransmitter Transporter Uptake Assay Kit (Molecular Devices) according to the manufacturer's instructions. Mature hDANs were seeded in Matrigel coated black, clear bottom 96-well plates prior to the assay at a density of 60,000/well in triplicates. Wells containing no cells were used as an internal control. hDANs were treated with a specific VMAT2 inhibitor (Tetrabenazine, 10µM), a TH inhibitor (3-Iondol-L-Tyrosine, 300µM), or a combination of MAO and COMT inhibitors (Tranylcypromine 10µM and Tolcapone 100nM respectively). These compounds were added in media containing L-DOPA (50µM) or without L-DOPA. A subset of hDANs triplicates were treated with media alone or media containing L-DOPA (50µM). All treatments were incubated on the cells at 37°C for 20 minutes prior to the addition of the substrates.

For the NT uptake in Figure 6G; hDANs were plated in the same way and either untreated or treated with 1mM BH4 for 2h prior to addition of substrates. Uptake fluorescence was measured using the SpectraMax M_2^e microplate reader in kinetic mode (Molecular Devices) measuring every 30s or as an endpoint after 30 minutes incubation with the substrates). After the assay, the hDANs were washed and fixed in 4% (v/v) PFA containing Hoechst to account for cell number in each well and then counterstained for TH to account for any large differences in TH positive hDANs in the culture wells. No outliers were removed. Statistics Figure 6E: Linear regression plotted, 2-way ANOVA was performed. Genotype across times was statistically significant ***=p<0.0001 nDiff=3. Figure 6F: In the presence of L-DOPA, THi and MAO/COMTi statistically significantly different to PINK1 KO hDANs using 2-way ANOVA (multiple comparisons). **=*p*0.0071 (*L-DOPA+THi, KO1), **=*p*0.0048 (*L-DOPA+THi, KO2), *=*p*0.049 (*L-DOPA+COMTi/MAOi, v KO1), **=*p*0.010 (*L-DOPA+COMTi/MAOi, v KO2) nDiff=3. Figure 6G: No outliers were removed. Neurotransmitter uptake was measured as a FL endpoint and normalized to the untreated control hDANs in each experiment, Welch's t test was performed. **=*p*0.0024 (untreated CTRL v PINK1 KO), *=*p*0.023 (untreated GC CTRL v PINK1 Q126P), ns=not significant. nDiff=3.

Monoamine oxidase (MAO) Activity Assay

MAO activity was monitored using a radiometric assay with ^{14}C-tyramine hydrochloride as substrate as previously described (Ugun-Klusek et al., 2019). Data were normalized for protein content and rates expressed as disintegrations of

14C/min/µg protein. The student's t test identified no significant differences. ns=not significant, nDiff=3.

Dopamine (Catecholamine) oxidation assay

The catecholamine oxidation assay was performed according to (Burbulla et al., 2017) using Biodyne® B 0.45µm membranes (Pall corporation) and detection using a LiCOR fluorescent scanning device. The quantification performed using Image Studio from LiCOR. Representative blots and standard curve are shown. Mean FL units were plotted for each genotype, fraction and treatment. No outliers were removed. The student's t tests were not significant (CTRL v PINK1 KO in each condition). 2-way ANOVA found significance across the genotypes (*=p0.144) including all the conditions. nDiff=3.

Supplementary Figures and Legends

Bus et al. Supplementary Figure 1

a

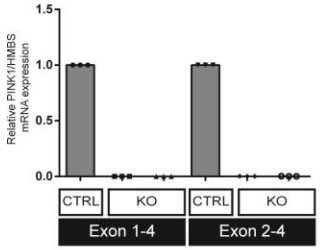

b

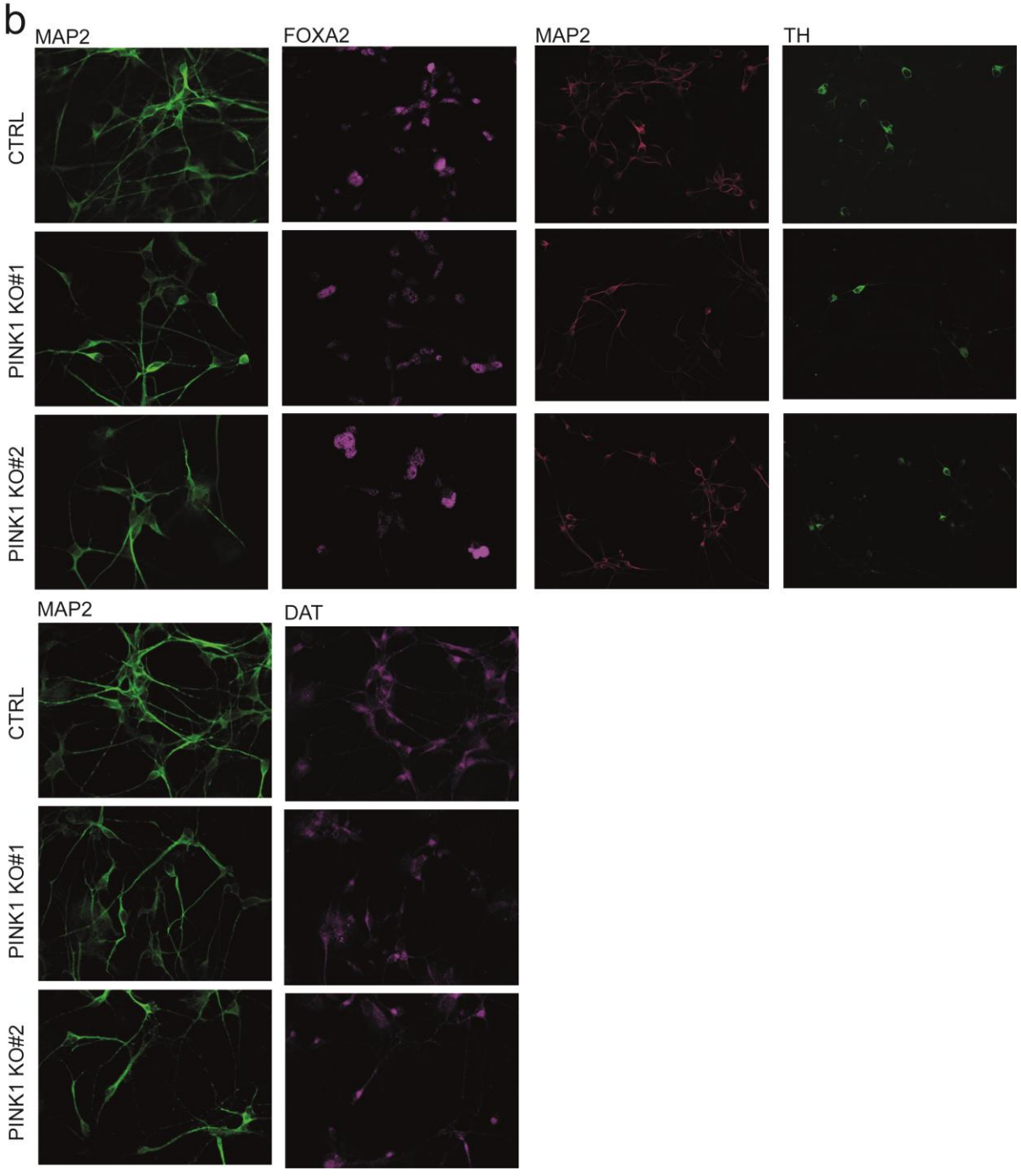

Supplementary Figure S1, related to Figure 1: S1A) Example immunocytochemistry staining of MAP2, TH and FOXA2 in fixed hDANs. Representative images are shown (nDiff=4). **S1B)** Relative PINK1 gene expression in control and PINK1 KO hDAN clones using primers directed to exon1-4 and exon 2-4 (nDiff=3).

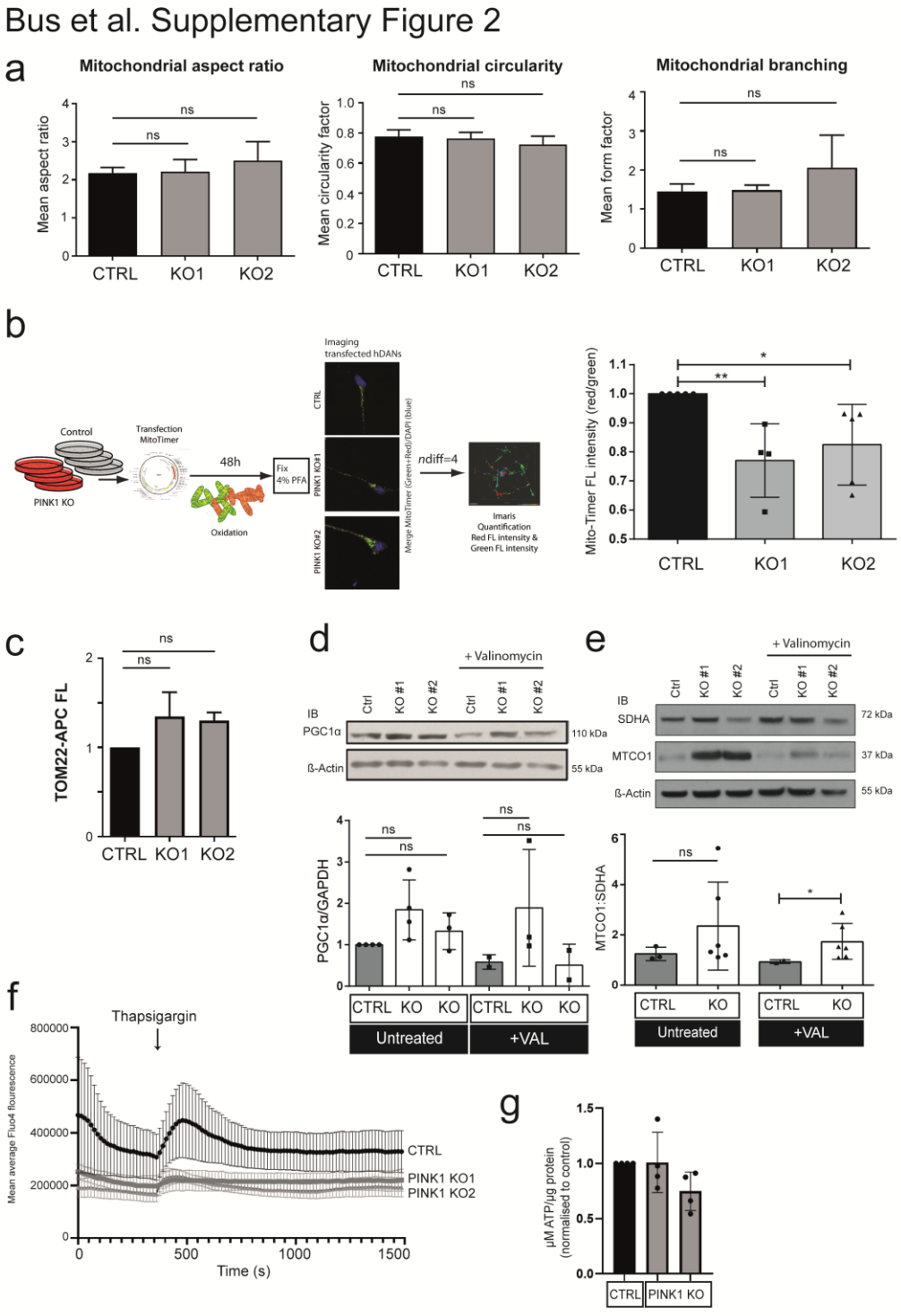

Supplementary Figure S2, related to Figure 2: S2A) Readouts of mitochondrial morphology in hDANs from live cell imaging (nDiff=3, ns=not significant). **S2B)** Diagram showing work flow for MitoTimer experiments in hDANs. Right panel: MitoTimer live cell imaging red/green fluorescence intensity ratio of PINK1 KO hDANs normalised to the isogenic control **=p0.0043 and *=p0.0222 (nDiff=3, error bars=SD). **S2C)** Tom22 fluorescence (APC-FL) detected by inside staining and flow cytometry in hDANs. ns=not significant (nDiff=3, error bars=SD). **S2D)** Upper panel respective Western blot of PGC1alpha in PINK1 KO hDANs and isogenic control under untreated conditions (UT) or valinomycin (VAL) 1µM, 24h (UT n=diff3-4; VAL n=2-3diff, error bars=SD). Lower panel densiometric quanitification of PGC1alpha signal normalised to GAPD and isogenic control. ns=not significant. **S2E)** Upper panel respective Western blot of SDHA and MTCO1 in PINK1 KO hDANs and healthy control under untreated conditions or valinomycin (VAL) 1µM, 24h (nDiff=3-5). Lower panel densiometric signal ratio of MTCO1/SDHA of PINK1 KO hDANs and healthy control (ns= not significant, *=p<0.05, error bars=SD). **S2F)** Total corrected cell Fluo4 fluorescence (cytosolic calcium) calculated for every live image frame across 1500 seconds (nDiff=4, error bars=SD) for CTRL and PINK1 KO hDANs. **S2G)** Normalised ATP levels in CTRL and PINK1 KO hDANs (nDiff=4, error bars =SD, T-test).

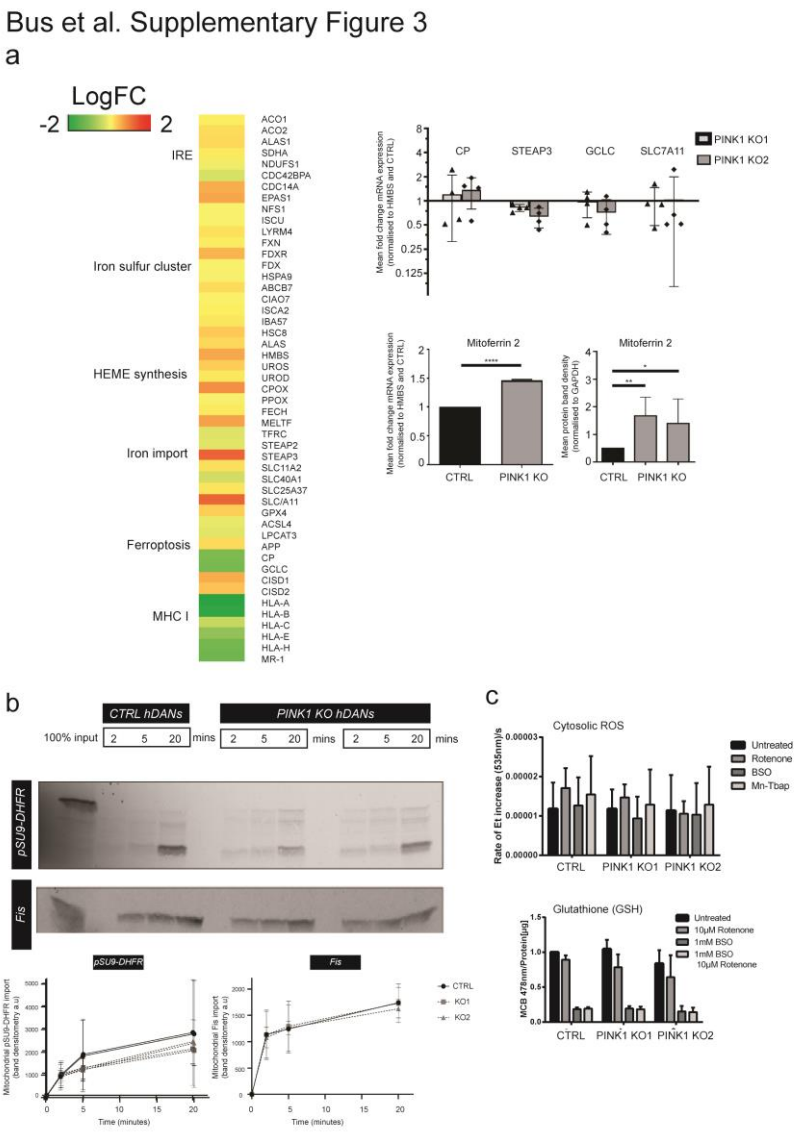

Supplementary Figure S3, related to Figure 3 A-F: S3A) Left panel: Genes identified from RNA sequencing related to iron metabolism. Log2FC values are shown for PINK1 KO hDAN clonal lines versus isogenic control (n=3, nDiff=1). Right panel: Mean fold change of mRNA expression of iron related genes; *CP*, *STEAP3*, *GCLC*, *SLC7A11* in PINK1 KO hDANs normalised to healthy control and HMBS (nDiff=4, error bars=SD). Lower panel: Expression of Mitoferrin-2. mRNA in PINK1 KO hDANs and isogenic control determined by qRT-PCR, results in mean fold change normalised to HMBS and control (nDiff=3; ****=p<0.0001). Western blot of Mitoferrin-2 in PINK1 KO hDANs compared to healthy control, mean protein band density normalised to GAPDH (nDiff=3-5, *=p<0.0179 **=p<0.0079). **S3B)** SDS–PAGE/ autoradiography analysis showing import of radiolabelled proteins 5S-pSU9-DHFR and ^{35}S-

Fis1 in PINK1 KO and healthy control hDANs after different time points (2, 5 and 20 min), arrows indicate precursor and mature pSU9-DHFR protein (nDiff=4, error bars=SD). **S3C)** Top panel: Mean rates of oxidised DiHET (Et) fluorescence signal increase (Ex 535nm/Em 610) per sec in PINK1 KO and isogenic control hDANs untreated or treated with 10µM Rotenone/ 1mM BSO/ 50µM Mn-Tbap indicating cytosolic ROS (nDiff=3, error bars=SD). Bottom panel: Fluorescence signal increase of MCB-GSH adduct in PINK1 KO hDANs and isogenic control untreated or treated with 10µM Rotenone/ 1mM BSO/ 1mM BOS + 10µM Rotenone (nDiff=3). Values normalised per µg protein of cell lysates and to untreated healthy control.

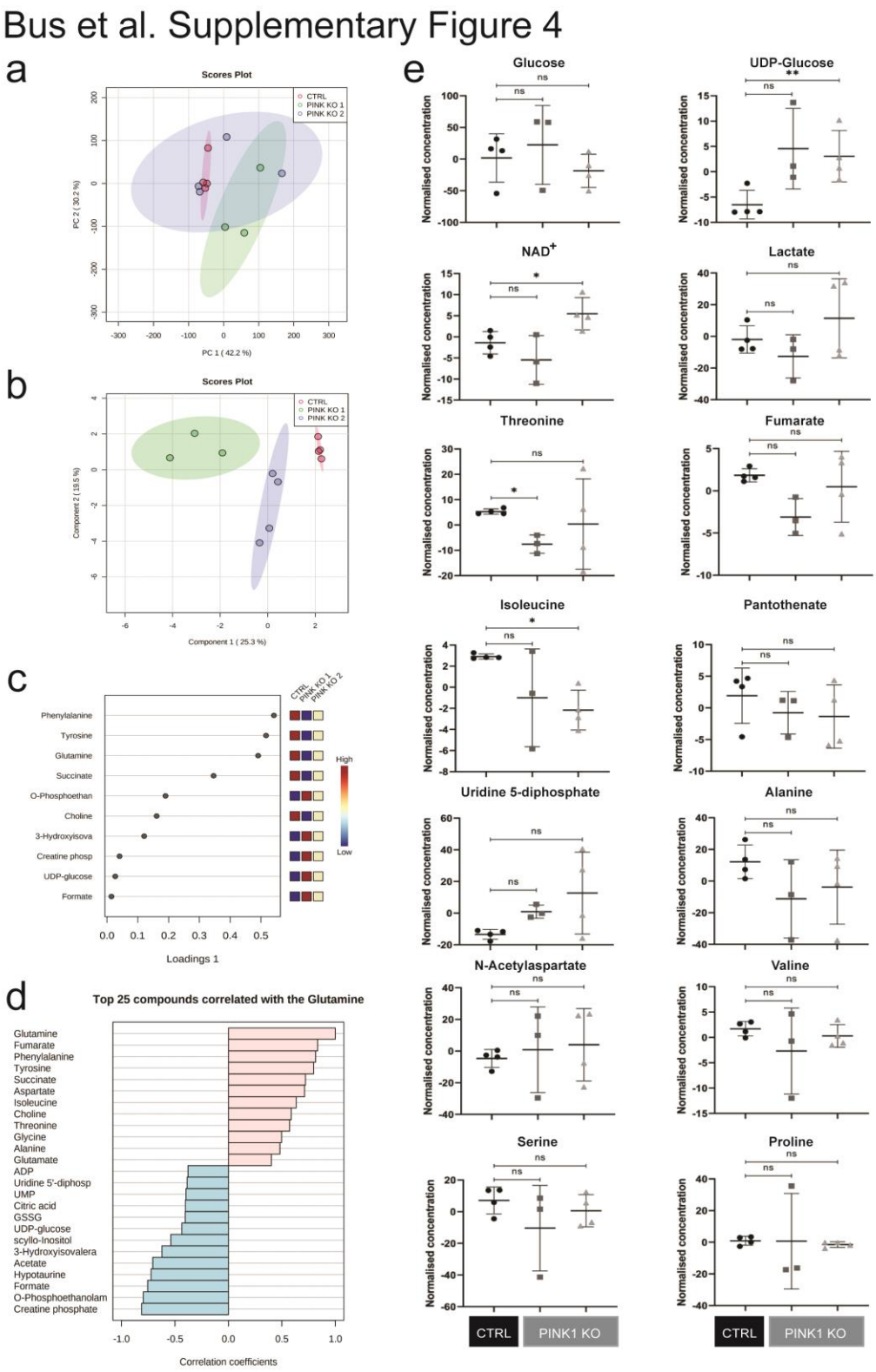

Supplementary Figure S4, related to Figure 3G-I: S4A) Principal Component Analysis (PCA) was generated for the control, KO 1 and 2 metabolomics data comparison. Generally, all three groups have strong similarities between the first two principal components since the

overlap is almost complete. **S4B)** Sparse partial least squares discriminant analysis (sPLS-DA) algorithm allowed reducing the dimensional complexity and illustrated the changes driven by most significant features of the groups. Here, the group separation is significantly improved which correlates to multiple metabolites having significant p-values. **S4C)** sPLS-DA loadings plot illustrates the metabolites which drive the group differences. Here, as top scoring metabolites are phenylalanine, tyrosine, glutamine and succinate, which we identify as main statistical significant metabolite changes. **S4D)** Pattern hunter was generated for glutamine and illustrated the top 25 metabolites which correlate the most strongly with this compound in the dataset (Pearson r distance measure). Glutamine concentration changes in this metabolic setup have the strongest correlation with fumarate, phenylalanine, tyrosine, succinate, aspartate, isoleucine, choline, threonine, glycine, alanine and glutamate, most of which are the amino acids supplying TCA cycle. **S4E)** Scatter plots were generated for all the metabolites of interest based on their changes between the control and KO groups. ns=not significant, *=p<0.05, **=p<0.005 (n=4, nDiff=2, error bars=SD).

Bus et al. Supplementary Figure 5

a

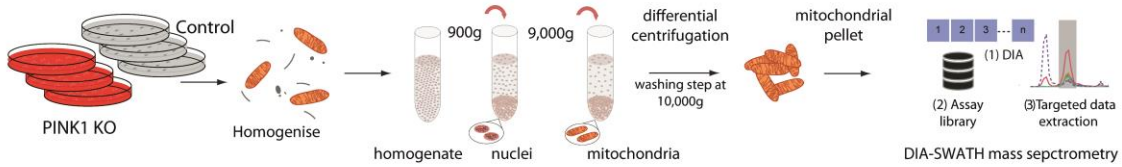

b

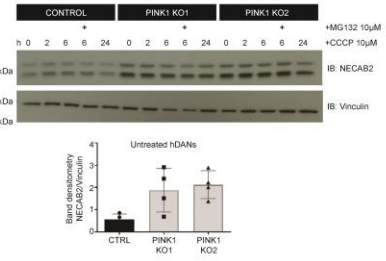

c

Diseases or Functions Annotation	p-value
Migration of cells	1,26E-07
Severe psychological disorder	3,26E-07
Mood Disorders	5,97E-07
Infarction	7,43E-07
Polyneuropathy	9,46E-07
Primary colorectal adenocarcinoma	9,66E-07
Primary colon carcinoma	9,66E-07
Autosomal dominant myopathy	1,08E-06
Peripheral neuropathy	1,76E-06
Healing of wound	2,40E-06
Hereditary motor neuropathy	2,78E-06

d

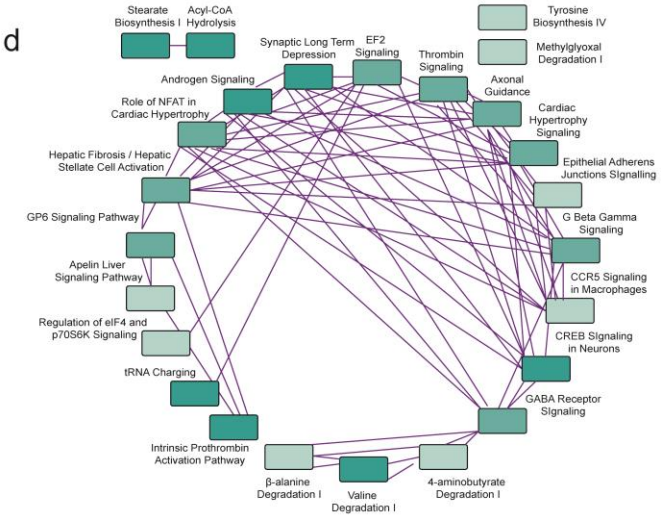

Supplementary Figure S5, related to Figure 5: S5A) Diagram of workflow and mitochondrial preparations from hDANs for quantitative mass spectrometry. **S5B)** Representative Western blot of NECAB2 (MitoNEET) and vinculin (loading control) in PINK1 KO hDANs and healthy control untreated or treated with 10µM CCCP for 0, 2, 6 (+/- 10µM MG132) for 24 hours. Densiometric quantification of NECAB2 Protein in untreated PINK1 KO hDANs and isogenic control normalized to Vinculin. Not significant. (nDiff=4, error bars=SD). **S5C)** Top annotate hits according to disease or function using Qiagen Ingenuity software. listed with respective *p* values. **S5D)** Plot of interactions between annotated biological pathways determined by Qiagen Ingenuity.

Supplementary References

ALLEN, G. F., ULLAH, Y., HARGREAVES, I. P., LAND, J. M. & HEALES, S. J. 2013. Dopamine but not l-dopa stimulates neural glutathione metabolism. Potential implications for Parkinson's and other dopamine deficiency states. *Neurochem Int,* 62**,** 684-94.

BLATTMANN, P., HEUSEL, M. & AEBERSOLD, R. 2016. SWATH2stats: An R/Bioconductor Package to Process and Convert Quantitative SWATH-MS Proteomics Data for Downstream Analysis Tools. *PLoS One,* 11**,** e0153160.

BRUDERER, R., BERNHARDT, O. M., GANDHI, T., MILADINOVIC, S. M., CHENG, L. Y., MESSNER, S., EHRENBERGER, T., ZANOTELLI, V., BUTSCHEID, Y., ESCHER, C., VITEK, O., RINNER, O. & REITER, L. 2015. Extending the limits of quantitative proteome profiling with data-independent acquisition and application to acetaminophen-treated three-dimensional liver microtissues. *Mol Cell Proteomics,* 14**,** 1400-10.

BURBULLA, L. F., SONG, P., MAZZULLI, J. R., ZAMPESE, E., WONG, Y. C., JEON, S., SANTOS, D. P., BLANZ, J., OBERMAIER, C. D., STROJNY, C., SAVAS, J. N., KISKINIS, E., ZHUANG, X., KRUGER, R., SURMEIER, D. J. & KRAINC, D. 2017. Dopamine oxidation mediates mitochondrial and lysosomal dysfunction in Parkinson's disease. *Science,* 357**,** 1255-1261.

CERMAK, T., DOYLE, E. L., CHRISTIAN, M., WANG, L., ZHANG, Y., SCHMIDT, C., BALLER, J. A., SOMIA, N. V., BOGDANOVE, A. J. & VOYTAS, D. F. 2011. Efficient design and assembly of custom TALEN and other TAL effector-based constructs for DNA targeting. *Nucleic Acids Res,* 39**,** e82.

CHOI, M., CHANG, C. Y., CLOUGH, T., BROUDY, D., KILLEEN, T., MACLEAN, B. & VITEK, O. 2014. MSstats: an R package for statistical analysis of quantitative mass spectrometry-based proteomic experiments. *Bioinformatics,* 30**,** 2524-6.

ESCHER, C., REITER, L., MACLEAN, B., OSSOLA, R., HERZOG, F., CHILTON, J., MACCOSS, M. J. & RINNER, O. 2012. Using iRT, a normalized retention time for more targeted measurement of peptides. *Proteomics,* 12**,** 1111-21.

FITZGERALD, J. C., ZIMPRICH, A., BERRIO, D. A. C., SCHINDLER, K. M., MAURER, B., SCHULTE, C., BUS, C., HAUSER, A. K., KUBLER, M., LEWIN, R., BOBBILI, D. R., SCHWARZ, L. M., VARTHOLOMAIOU, E., BROCKMANN, K., WUST, R., MADLUNG, J., NORDHEIM, A., RIESS, O., MARTINS, L. M., GLAAB, E., MAY, P., SCHENKE-LAYLAND, K., PICARD, D., SHARMA, M., GASSER, T. & KRUGER, R. 2017. Metformin reverses TRAP1 mutation-associated alterations in mitochondrial function in Parkinson's disease. *Brain,* 140**,** 2444-2459.

GLOECKNER, C. J., SCHUMACHER, A., BOLDT, K. & UEFFING, M. 2009. The Parkinson disease-associated protein kinase LRRK2 exhibits MAPKKK activity and phosphorylates MKK3/6 and MKK4/7, in vitro. *J Neurochem,* 109**,** 959-68.

HARGREAVES, I. P., DUNCAN, A. J., WU, L., AGRAWAL, A., LAND, J. M. & HEALES, S. J. 2007. Inhibition of mitochondrial complex IV leads to secondary loss complex II-III activity: implications for the pathogenesis and treatment of mitochondrial encephalomyopathies. *Mitochondrion,* 7**,** 284-7.

HERNANDEZ, G., THORNTON, C., STOTLAND, A., LUI, D., SIN, J., RAMIL, J., MAGEE, N., ANDRES, A., QUARATO, G., CARREIRA, R. S., SAYEN, M. R., WOLKOWICZ, R. & GOTTLIEB, R. A. 2013. MitoTimer: a novel tool for monitoring mitochondrial turnover. *Autophagy,* 9**,** 1852-61.

PIERIK, A. J., NETZ, D. J. & LILL, R. 2009. Analysis of iron-sulfur protein maturation in eukaryotes. *Nat Protoc,* 4**,** 753-66.

PRESTEL, J., GEMPEL, K., HAUSER, T. K., SCHWEITZER, K., PROKISCH, H., AHTING, U., FREUDENSTEIN, D., BUELTMANN, E., NAEGELE, T., BERG, D., KLOPSTOCK, T. & GASSER, T. 2008. Clinical and molecular characterisation of a Parkinson family with a novel PINK1 mutation. *J Neurol,* 255**,** 643-8.

REINHARDT, P., GLATZA, M., HEMMER, K., TSYTSYURA, Y., THIEL, C. S., HOING, S., MORITZ, S., PARGA, J. A., WAGNER, L., BRUDER, J. M., WU, G., SCHMID, B., ROPKE, A., KLINGAUF, J., SCHWAMBORN, J. C., GASSER, T., SCHOLER, H. R. & STERNECKERT, J. 2013. Derivation and expansion using only small molecules of human neural progenitors for neurodegenerative disease modeling. *PLoS One,* 8**,** e59252.

ROST, H. L., AEBERSOLD, R. & SCHUBERT, O. T. 2017. Automated SWATH Data Analysis Using Targeted Extraction of Ion Chromatograms. *Methods Mol Biol,* 1550**,** 289-307.

SCHUBERT, O. T., GILLET, L. C., COLLINS, B. C., NAVARRO, P., ROSENBERGER, G., WOLSKI, W. E., LAM, H., AMODEI, D., MALLICK, P., MACLEAN, B. & AEBERSOLD, R. 2015. Building high-quality assay libraries for targeted analysis of SWATH MS data. *Nat Protoc,* 10**,** 426-41.

TYANOVA, S., TEMU, T. & COX, J. 2016. The MaxQuant computational platform for mass spectrometry-based shotgun proteomics. *Nat Protoc,* 11**,** 2301-2319.

UGUN-KLUSEK, A., THEODOSI, T. S., FITZGERALD, J. C., BURTE, F., UFER, C., BOOCOCK, D. J., YU-WAI-MAN, P., BEDFORD, L. & BILLETT, E. E. 2019. Monoamine oxidase-A promotes protective autophagy in human SH-SY5Y neuroblastoma cells through Bcl-2 phosphorylation. *Redox Biol,* 20**,** 167-181.

WOLBURG-BUCHHOLZ, K., MACK, A. F., STEINER, E., PFEIFFER, F., ENGELHARDT, B. & WOLBURG, H. 2009. Loss of astrocyte polarity marks blood-brain barrier impairment during experimental autoimmune encephalomyelitis. *Acta Neuropathol,* 118**,** 219-33.